

# Supporting information for: Single molecule junctions based on nitrile terminated biphenyls: A new promising anchoring group

Artem Mishchenko,<sup>†</sup> Linda A. Zotti,<sup>‡</sup> David Vonlanthen,<sup>¶</sup> Marius Bürkle,<sup>§</sup> Fabian Pauly,<sup>§</sup> Juan Carlos Cuevas,<sup>\*,‡</sup> Marcel Mayor,<sup>\*,¶</sup> and Thomas Wandlowski<sup>\*,†</sup>

*Department of Chemistry and Biochemistry, University of Bern, CH-3012 Bern, Switzerland, Departamento de Física Teórica de la Materia Condensada, Universidad Autónoma de Madrid, E-28049 Madrid, Spain, Department of Chemistry, University of Basel, CH-4003 Basel, Switzerland, and Institut für Theoretische Festkörperphysik, Karlsruhe Institute of Technology (KIT), D-76131 Karlsruhe, Germany*

E-mail: juancarlos.cuevas@uam.es; marcel.mayor@unibas.ch; thomas.wandlowski@dcb.unibe.ch

## Experimental

### STM-based single molecule conductance measurement

The conductances of single-molecule junctions were studied using an scanning-tunneling-microscopy-based break junction (STM-BJ) approach for measuring the current through a molecule trapped

---

\*To whom correspondence should be addressed

<sup>†</sup>University of Bern

<sup>‡</sup>Universidad Autónoma de Madrid

<sup>¶</sup>University of Basel

<sup>§</sup>Karlsruhe Institute of Technology (KIT)

between STM tip and sample substrate. The experimental approach was described in detail in our previous publication.<sup>1</sup>

The sample substrates were both Au(111) single crystals and Au (111) films on glass wafers. No differences in the results were found. The Au(111) substrates were flame-annealed prior to use. 1 mM solutions of the studied molecules were freshly prepared in a 4:1 mixture of 1,3,5-trimethylbenzene (mesitylene, 98%, Aldrich) and tetrahydrofuran (THF, 99.9%, Aldrich). The gold STM tips were prepared by electrochemical etching of gold wires (99.999%, 0.25 mm diameter). All experiments were carried out at room temperature under argon atmosphere using a modified Molecular Imaging PicoSPM. The standard STM scanner was replaced by an STM scanner with a modified dual channel preamplifier.<sup>2</sup> The input current was simultaneously converted to two voltage signals with the conversion factors 21  $\mu\text{A/V}$  (high range) and 10 nA/V (low range). Both signals were split, and the original as well as the 10 times amplified signals were recorded, both original channels were also digitally zoomed in, which gives in total 6 channels.

The STM-BJ experiments were carried out according to the following procedure. After approach of the STM tip to the gold surface a few images were recorded in order to check the cleanliness of the sample. Current-distance measurements were then performed with the STM feedback switched off and the vertical tip movement controlled by the analog ramp unit described elsewhere.<sup>2</sup> In the measuring cycle, first the controlling software drives the STM tip toward the surface. Simultaneously the current through the junction is monitored. The approach was stopped when a pre-defined upper current limit was reached. Under the present experimental conditions with molecule-containing solutions the latter was typically 160  $\mu\text{A}$  (ca.  $10 - 20G_0$ ). After a short ( $\approx 20$  ms) delay, ensuring tip relaxation and formation of stable contacts, the tip was withdrawn by several nanometers (typically 5–10 nm). Approaching and withdrawing of the tip were performed with a rate of about 60  $\text{nm}\cdot\text{s}^{-1}$ . The current-time traces were recorded during the withdrawing step with a digital oscilloscope (Yokogawa DL750) triggered by a current drop below 20  $\mu\text{A}$ . The above cycle was repeated in several series of  $\approx 2000$  traces at each set of experimental conditions to ensure the statistical significance of the results. For each molecule the data were recorded at three different bias voltages

of 0.065 V, 0.100 V and 0.170 V.

## Data analysis

### 1D conductance histograms

The raw data were analyzed with a lab-made software implemented in LabView 8.6. The program works with the raw data saved in binary format (.wvf) via using the header description file (.hdr) of a Yokogawa oscilloscope. First, the offset of all 6 channels were nullified by fitting Gaussian distribution to a single curve histogram in the noise level. Then, after multiplication by the gain factor, all six channels were combined in the linear scale. Only part of the curve between  $10G_0$  and  $10^{-7}G_0$  was used further. After taking the logarithm and binning, the histogram was constructed. Histograms of all curves are added together and saved as ASCII file. The histograms composed of all measured curves were built in this way without any data selection (see, e.g. Figure S5). The feature around  $\log(G/G_0) = -2$  (asterisk in Figure S5a) in all conductance histograms shown is an artifact produced by the fast diode analog switch in the electronic circuit used in our dual-channel preamplifier.<sup>2</sup> The shoulder around  $\log(G/G_0) = -6$  (arrow in Figure S5a) represents the noise level of our dual-channel preamplifier.

Sometimes this shoulder can form a peak-like shape close to  $\log(G/G_0) = -6$  because traces were cut once the conductance dropped below  $\log(G/G_0) = -7$ . Compare, e.g. the two histograms in Figure S1, where the red-colored histogram was obtained with cutting at  $\log(G/G_0) = -7$ , which represents the noise level of our current setup. The blue-colored histogram was constructed from individual traces, which contain 5000 more data points in the “noisy region”, i.e. the part of the trace below  $\log(G/G_0) = -7$ .

### Characteristic length histogram

We introduce a “characteristic length” as the difference in  $z$  values between two preset conductance values  $G_1$  and  $G_2$  as  $z(G_2) - z(G_1)$  with  $G_1$  approximately one order of magnitude higher than the

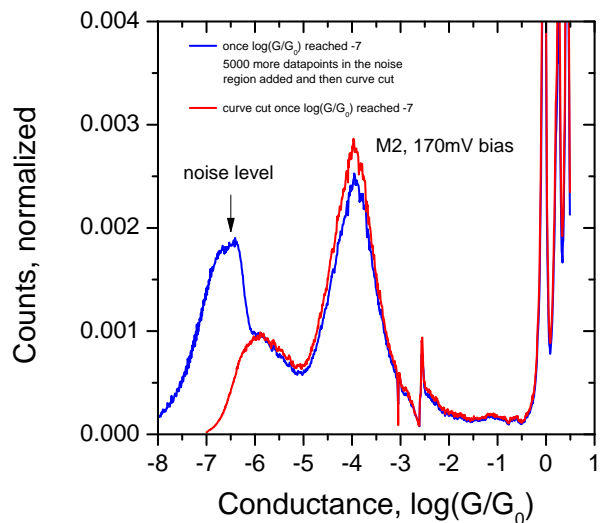


Figure S1: Conductance log-histograms of M2, 170 mV bias. The red curve is the same as in Figure S12a, i.e. constructed after cutting the noise level. The blue curve was obtained from the same data, but without cutting the noise level.

molecular conductance peak in the 1D conductance histogram ( $G_{max}$ ), and  $G_2$  approximately one order of magnitude lower than  $G_{max}$ , i.e.  $G_1$  and  $G_2$  are sufficiently higher and lower than the typical variation of the molecular conductance (i.e. at the beginning and at the end of the conductance peak), see Figure S2. The following algorithm was applied: firstly, the range of the single molecule conductances ( $G_1$  and  $G_2$  values) was extracted from the conductance histogram, Figure S2A. Then, the number of data points between the highest and the lowest conductance values was measured for each curve and converted to a length by using the piezo conversion coefficient and the sampling rate of the oscilloscope. After processing of all curves the histogram was built from the frequency count of all respective length values, Figure S2C.

For example, the results presented for M4 in the main text (Fig. 1B, inset) were obtained with the limits  $G_1 = 3 \cdot 10^{-4}G_0$  and  $G_2 = 3 \cdot 10^{-6}G_0$ . The results do not change significantly upon variation of  $G_1$ , because  $G_1$  is typically localized in the steeply decreasing part of the conductance-distance trace, just after breaking the last Au-Au contact, and before a molecule is trapped in the junction. As a consequence the analysis is rather insensitive to the specific value of  $G_1$ , provided that  $G_1 > G_{max}$ . The choice of the lower limit,  $G_2$ , is more critical and influences directly the shape of the length

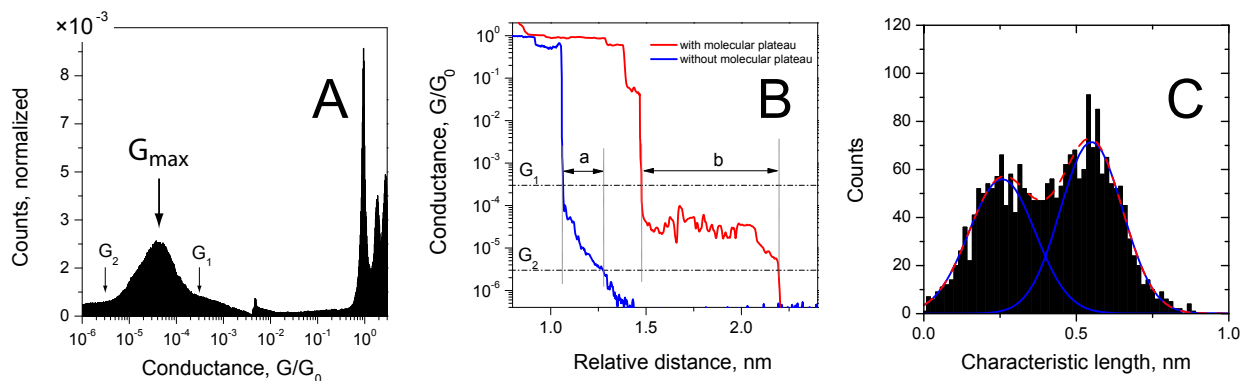


Figure S2: Characteristic length analysis scheme.

histogram. The influence of  $G_2$  on the characteristic length histogram for M4 is presented in Figure S3.

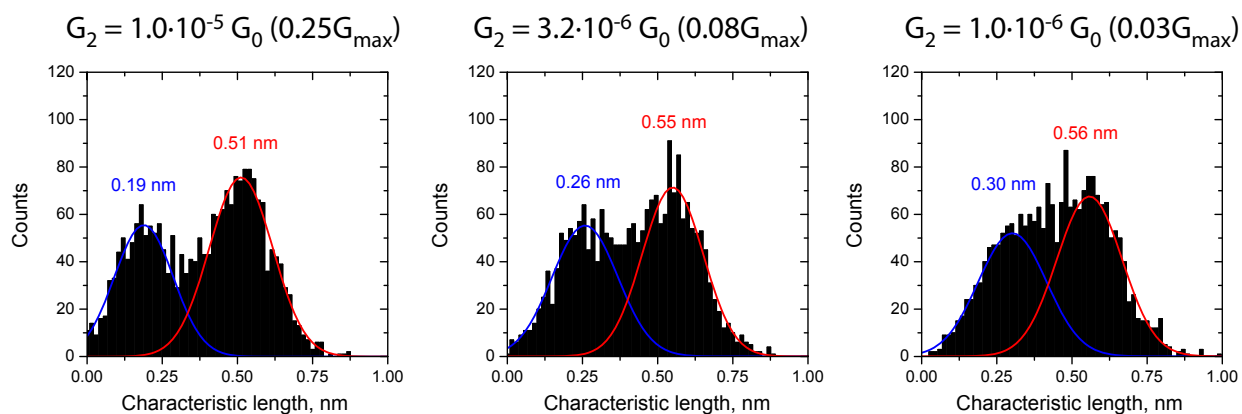


Figure S3: Influence of the parameter  $G_2$  on the characteristic length analysis. M4 is chosen as an example (cf. Figure 1b, main text) with  $G_1 = 1 \cdot 10^{-3} G_0$  kept fixed.

Figure S3 displays two maxima. The first one depends on  $G_2$  and shifts from 0.19 to 0.30 nm, while the second one is rather insensitive to the variation of  $G_2$ . We attribute the first peak to the average tip traveling distance required for the tunneling current to drop from  $G_1$  to  $G_2$  without the formation of molecular junctions (distance **a** in Figure S2B). The second peak (or shoulder in some cases) at around 0.5 nm is rather independent of the choice of  $G_2$  because of the sharp decrease in the conductance after a previously formed molecular plateau is broken (distance **b** in Figure S2B). In consequence we assign the second peak to the “true” average length of a molecular plateau.

In summary, the dependence of the characteristic length histogram on the conductance limits

$G_1$  and  $G_2$  provides an objective criterion in our all-data-point analysis to discriminate between tunneling features and “true” molecular conductance junctions.

## **2D conductance-length histogram**

The raw data were analyzed with a lab-made software implemented in LabView 8.6. The program works with the raw data saved in binary format (.wv $\epsilon$ ) via using the header description file (.hdr) of a Yokogawa oscilloscope. First, the offsets of all 6 channels were nullified by fitting a Gaussian distribution to a single curve histogram in the noise level. Then, after multiplication by the gain, all six channels were combined in the linear scale, and after taking the logarithm it leads to the Y-axis of the conductance-distance trace. The X-axis of the conductance-distance traces is obtained from the number of data points, the piezo conversion coefficient and the sampling rate of the oscilloscope. The X-axis is normalized with respect to the  $G_0$  rupture. Usually we set  $z = 0$  at  $G = 0.7G_0$ . The individual conductance-distance traces obtained in this manner were binned in 2D space (usually  $1000 \times 1000$  bins) and the resulting 2D conductance-length histograms were plotted as intensity graphs. Then all individual 2D histograms were added together and the result represents statistically significant conductance-distance trends (see, e.g. Figure S6).

## **Covariance matrix**

The development of this data analysis strategy was inspired by the work of Halbritter et al.<sup>3</sup> Briefly, we analyze the covariance between different parts of the conductance histogram. Covariance here provides a measure of the strength of the correlation between two different parts of a 1D conductance histogram. In other words, the covariance analysis can help to see whether different parts of the histogram are correlated with each other. For example, if  $1G_0$ ,  $2G_0$  and  $3G_0$  peaks are simultaneously present in most of the single trace histograms, this will lead to positive covariance values at  $1G_0 \times 2G_0$ ,  $1G_0 \times 3G_0$  and  $2G_0 \times 3G_0$ , see Figure S4 as an example. Another example can be a molecule with a clear conductance step (e.g. at  $10^{-4}G_0$ ) followed by sharp abrupt drop in conductance (e.g. until  $10^{-6}G_0$ ), the latter showing an exponentially decaying conductance in the

absence of molecules in region from  $10^{-4}G_0$  to  $10^{-6}G_0$ . Then there will be a negative covariance in the region  $10^{-4}G_0 \times (10^{-5} - 10^{-6})G_0$ . In other words, with the help of the covariance analysis one can extract information which is hidden in 1D and/or 2D conductance histograms.

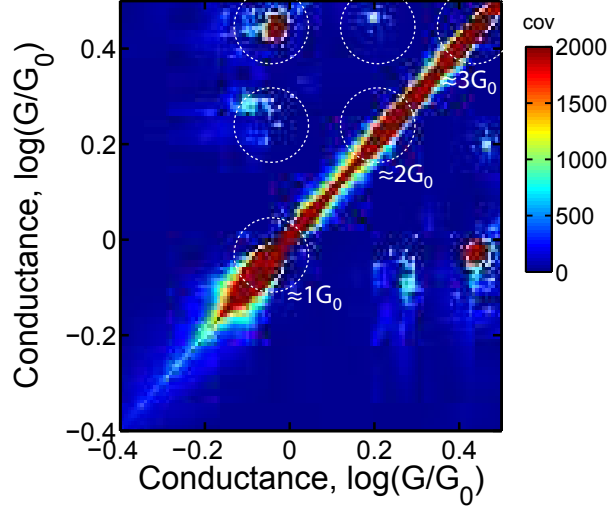


Figure S4: Covariance matrix of the conductance of M4,  $V_{\text{bias}} = 170 \text{ mV}$ . Region in the gold-gold contact is zoomed in. Positive covariance around  $1G_0 \times 2G_0$ ,  $1G_0 \times 3G_0$  and  $2G_0 \times 3G_0$  is visible as red-colored spots.

We use the following procedure to build covariance histograms: we constructed individual 1D histograms of  $\log(G/G_0)$  with the same set of bins for each of the  $n$  measured stretching curves. The results are presented as amount of counts in bin  $i$  of the  $k$ -th curve  $C(k, i)$ . For  $n$  single curve histograms denoted  $C(k, i)$ , the covariance  $\text{cov}(i, j)$  between two bins with indices  $i$  and  $j$  is defined by

$$\text{cov}(i, j) = \mathbb{E}_k [(C(k, i) - \mathbb{E}_k C(k, i)) (C(k, j) - \mathbb{E}_k C(k, j))] \quad (1)$$

where  $\mathbb{E}_k$  represents recursive averaging,  $\mu(k, i)$ , over all single-curve histograms,  $k$  is the number of the histogram,  $i$  is the number of the bin:

$$\mathbb{E}_k \equiv \mu(k, i) = \frac{k-1}{k} \mu(k-1, i) + \frac{1}{k} C(k, i) \quad (2)$$

The matrix  $V_{ij}$  of the quantities  $V_{ij} = \text{cov}(i, j)$  called the covariance matrix was used to analyze

the covariability of the respective data. In this case the covariance  $V_{ij}$  is a measure of how much two bins  $(i, j)$  change simultaneously. One obtains  $V_{ij} = 0$ ,  $V_{ij} > 0$  or  $V_{ij} < 0$ , depending if they are independent of each other, change simultaneously (increase or decrease in the same direction), or tend to change in opposite directions. For  $i = j$  we obtain the variance  $V_{i=j} \equiv \mathbf{Var}(C_{i=j}) = \mathbb{E} \left[ (C_{i=j} - \mathbb{E}C_{i=j})^2 \right]$ .

## Results

### Biphenyl Dinitrile M1 N#Cc1ccc(cc1)-c2ccc(cc2)C#N

Conductance histograms for M1 at  $V_{\text{bias}} = 100 \text{ mV}$  (Figure S5a) and  $V_{\text{bias}} = 65 \text{ mV}$  (Figure S5b) show a sharp pronounced peak around  $5\text{--}6 \times 10^{-5} G/G_0$ . The feature around  $\log(G/G_0) = -2$  (asterisk in Figure S5a) in all conductance histograms shown is an artifact produced by the fast diode analog switch in the electronic circuit used in our dual-channel preamplifier.<sup>2</sup> The shoulder around  $\log(G/G_0) = -6$  (arrow in Figure S5a) represents the noise level of our dual-channel preamplifier.

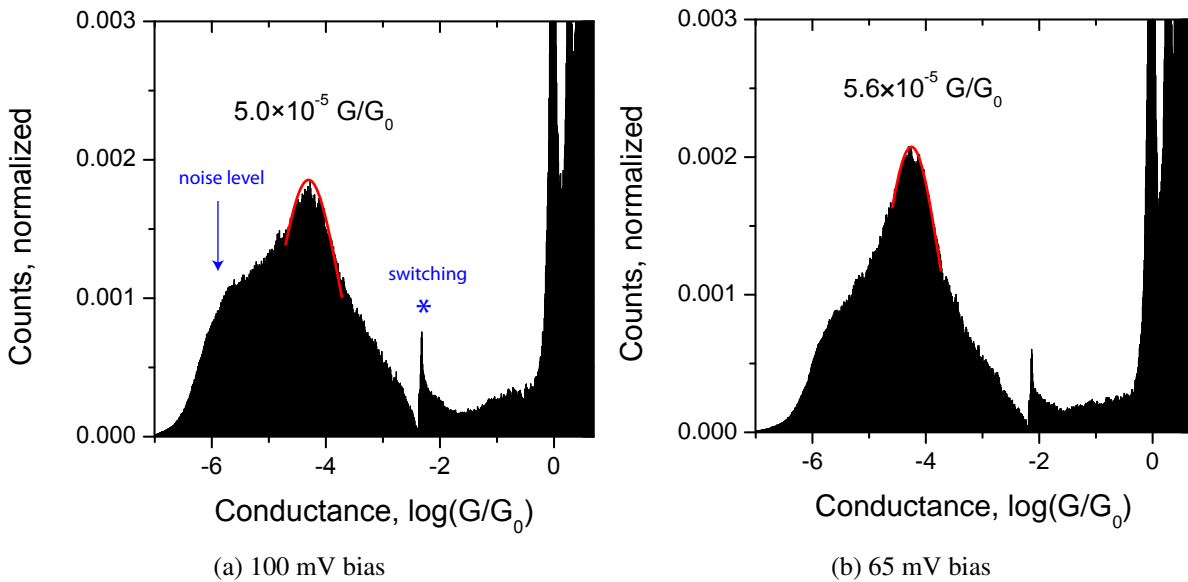


Figure S5: Conductance log-histograms of M1.

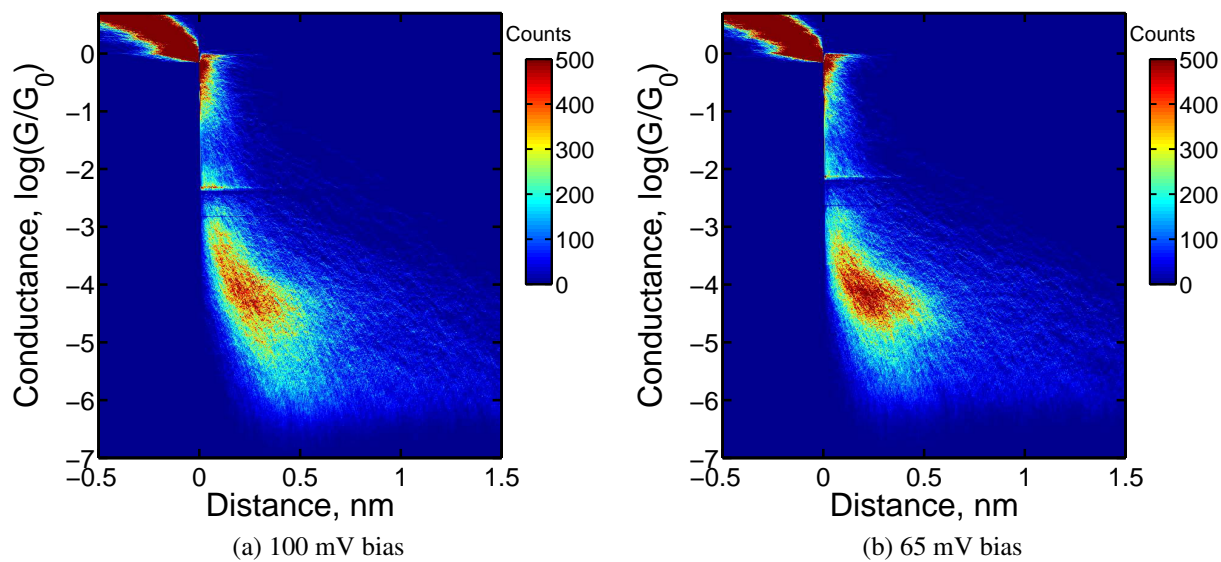


Figure S6: Conductance – distance 2D histograms of M1.

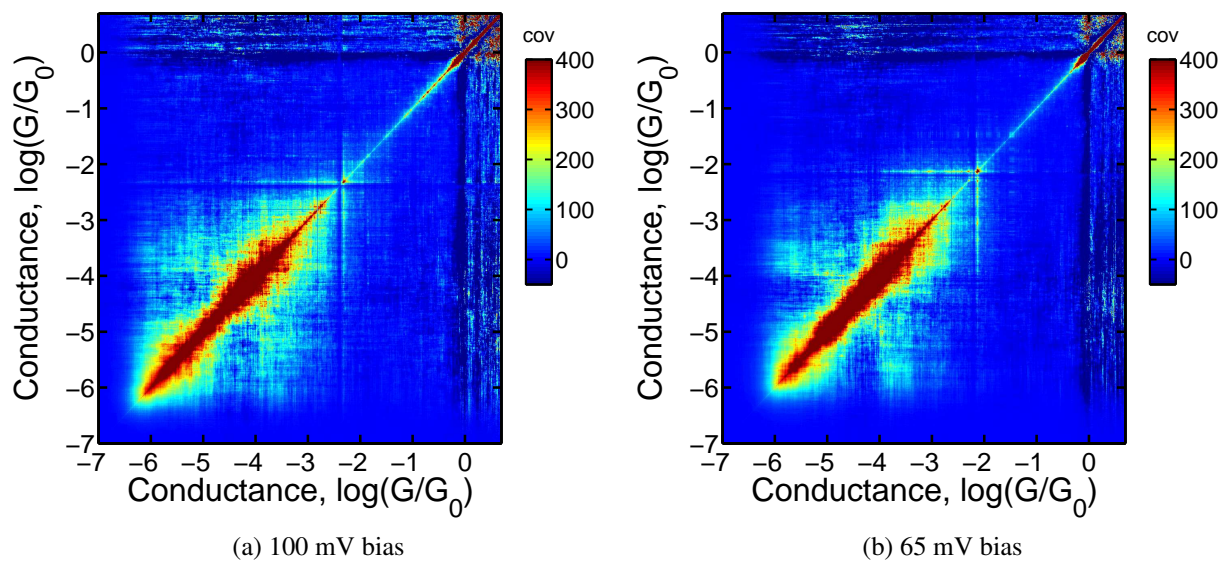
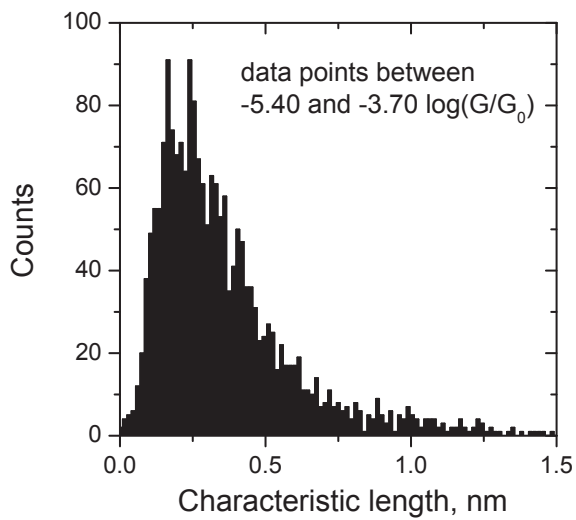
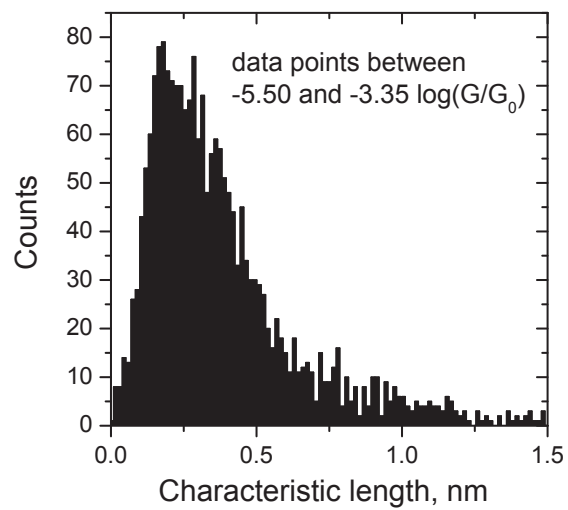


Figure S7: Covariance matrix of the conductance log-histogram of M1.

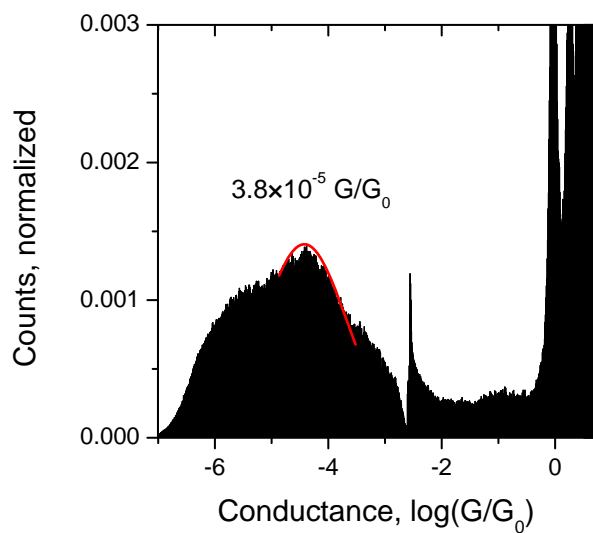


(a) 100 mV bias

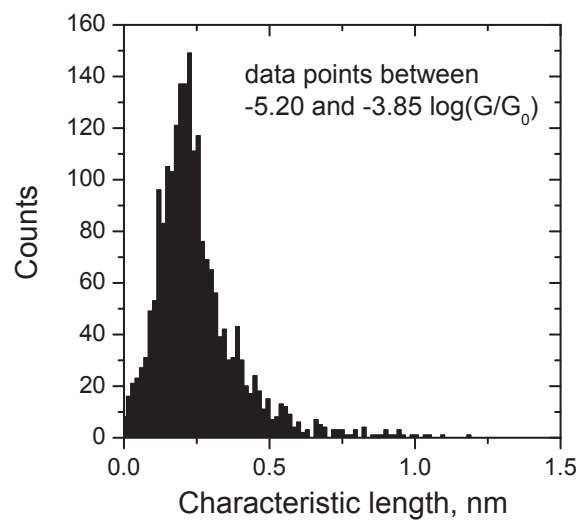


(b) 65 mV bias

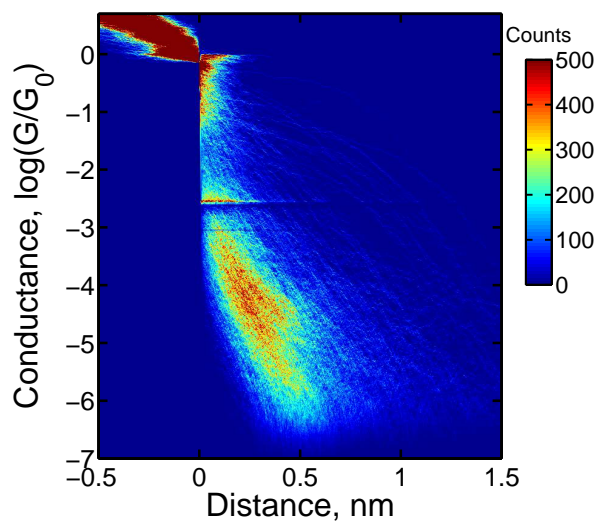
Figure S8: Characteristic length histogram of M1.



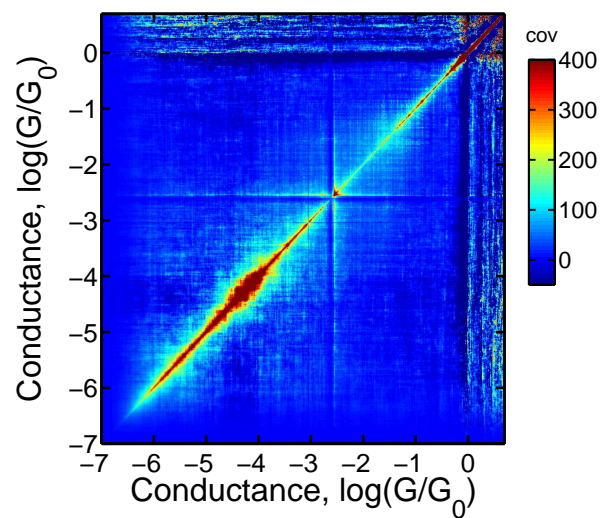
(a) Conductance histogram



(b) Characteristic length histogram



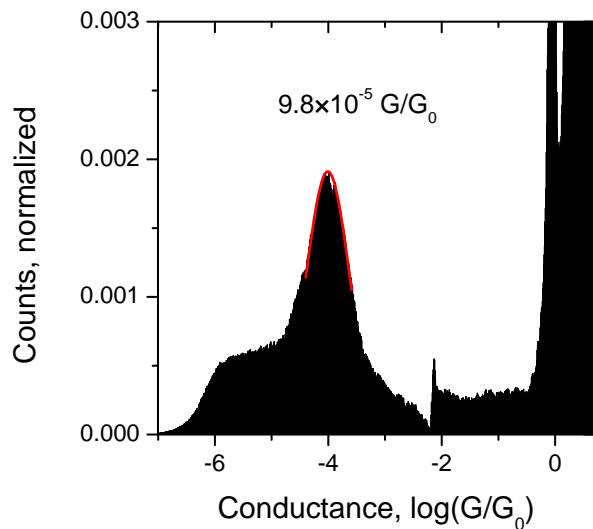
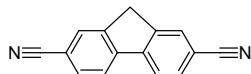
(c) 2D histogram



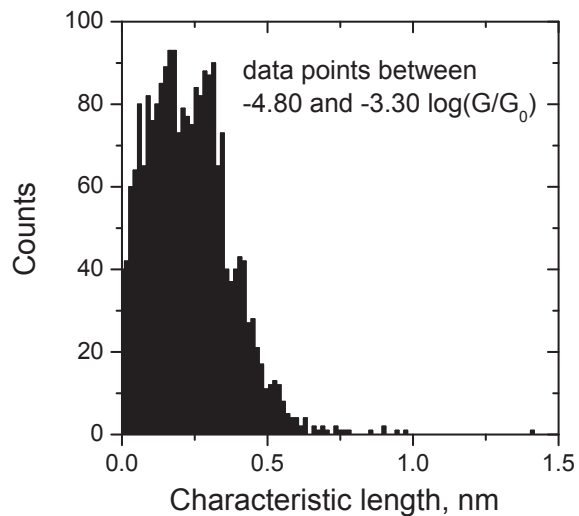
(d) Covariance matrix

Figure S9: Data analysis of the conductance of M1,  $V_{\text{bias}} = 170 \text{ mV}$ .

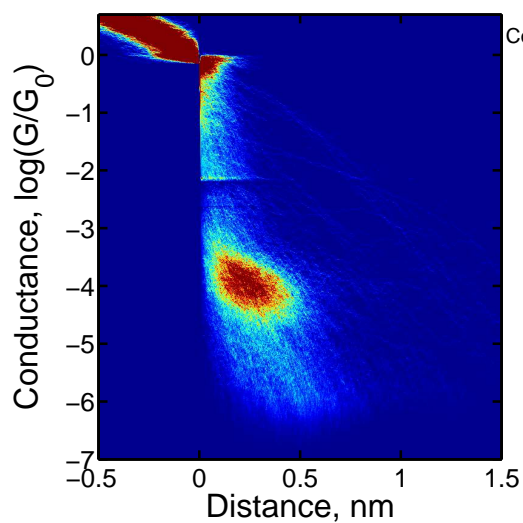
# Biphenyl dinitrile M2



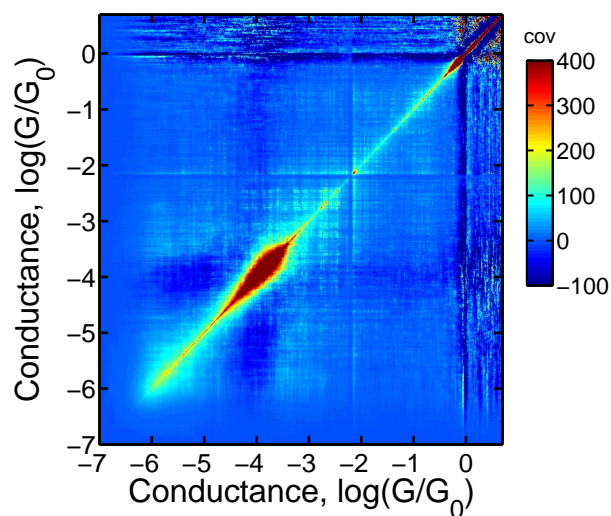
(a) Conductance histogram



(b) Characteristic length histogram

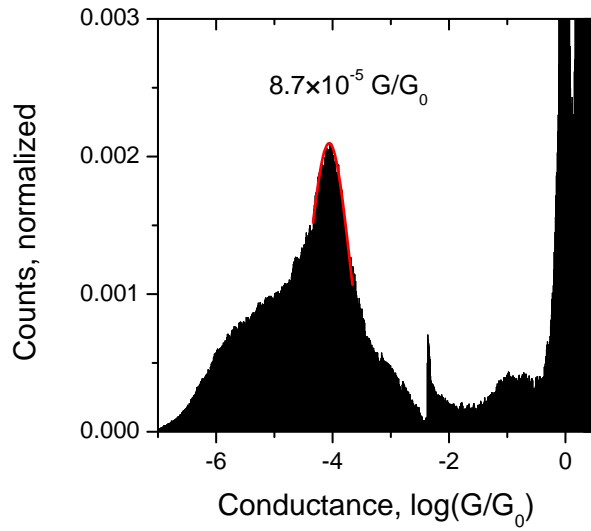


(c) 2D histogram

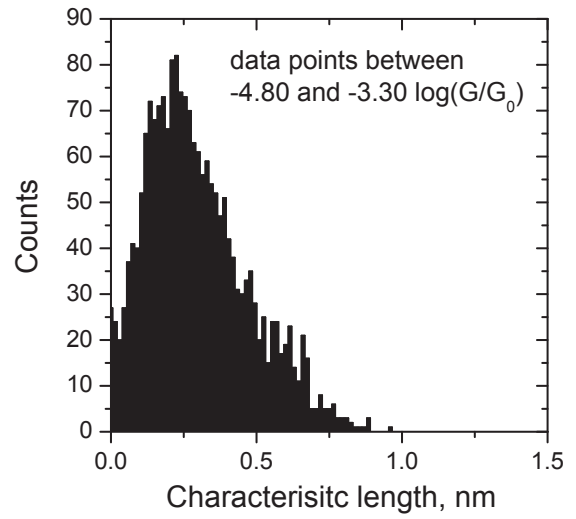


(d) Covariance matrix

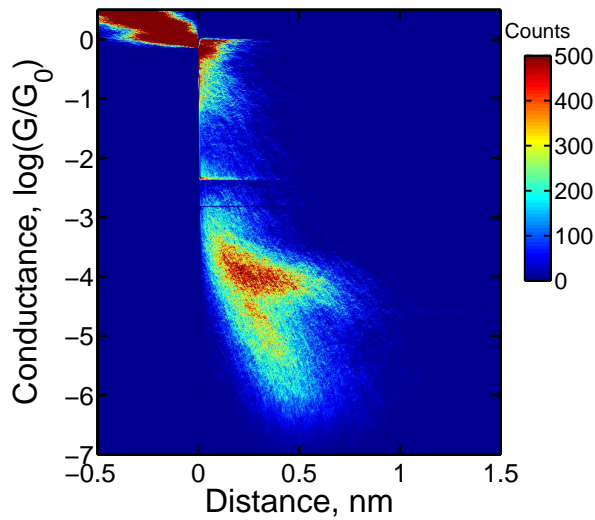
Figure S10: Data analysis of the conductance of M2,  $V_{\text{bias}} = 65$  mV.



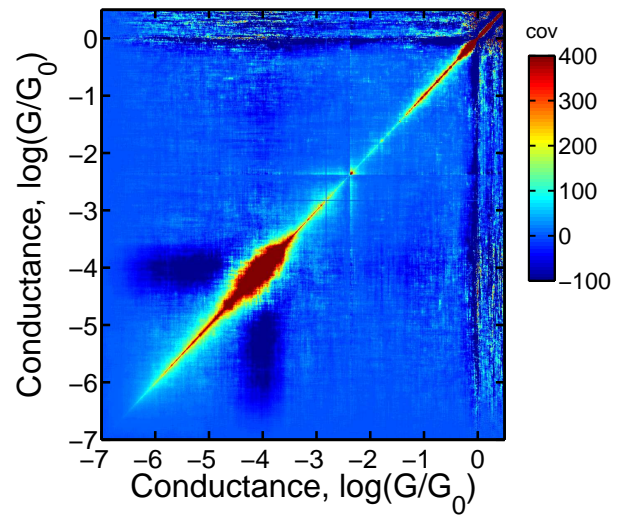
(a) Conductance histogram



(b) Characteristic length histogram

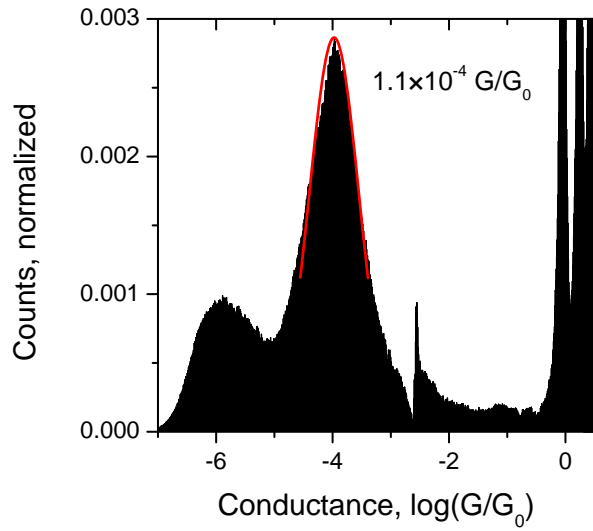


(c) 2D histogram

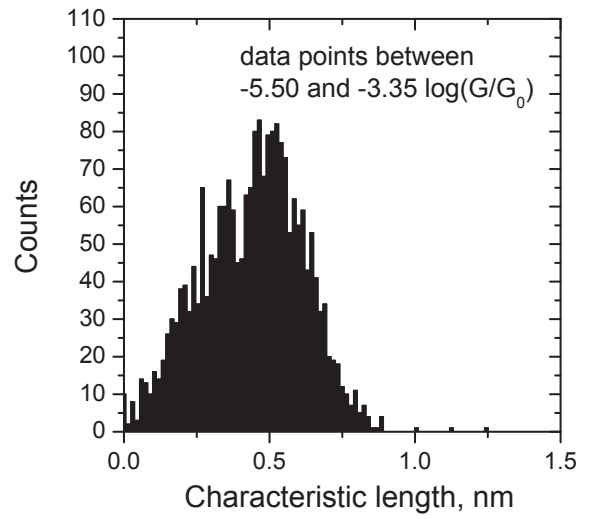


(d) Covariance matrix

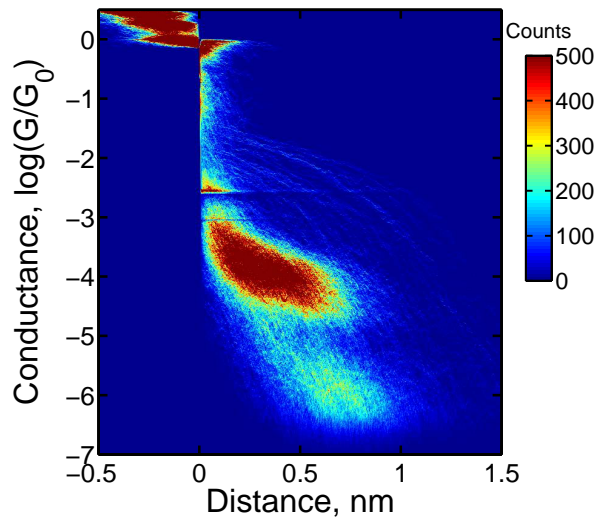
Figure S11: Data analysis of the conductance of M2,  $V_{\text{bias}} = 100 \text{ mV}$ .



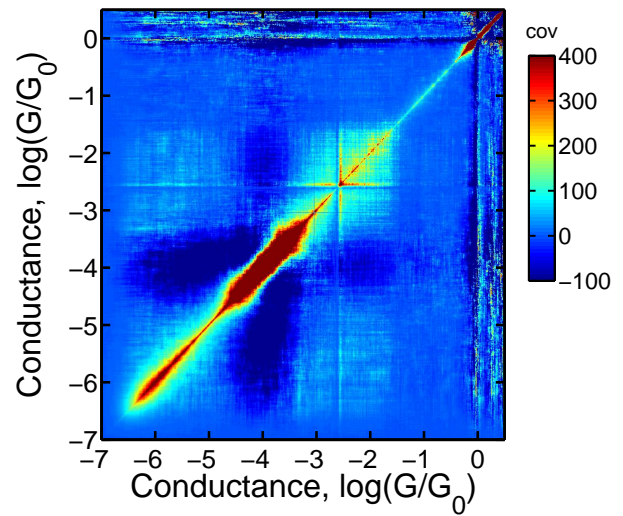
(a) Conductance histogram



(b) Characteristic length histogram



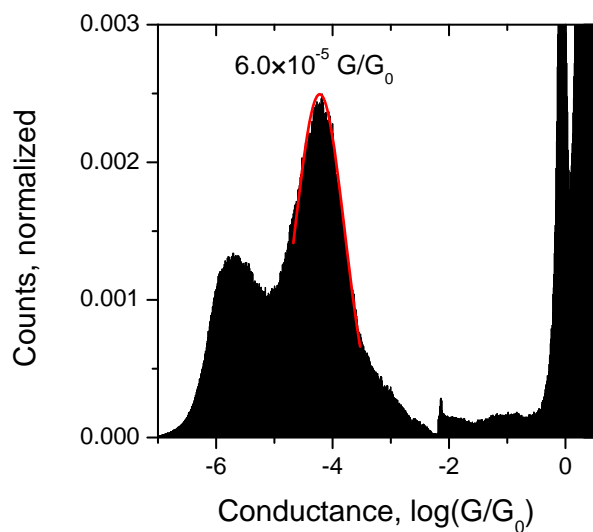
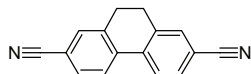
(c) 2D histogram



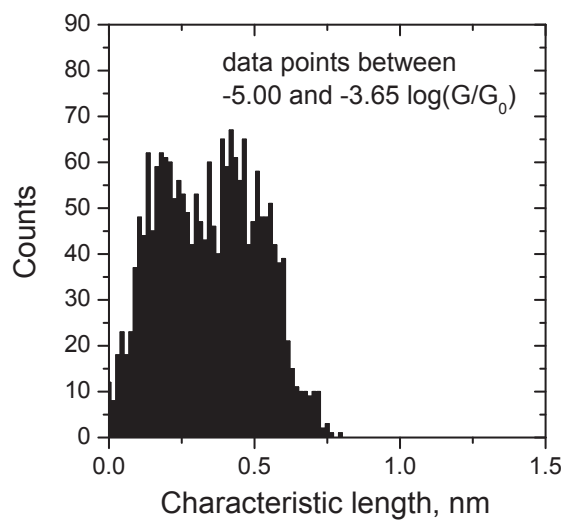
(d) Covariance matrix

Figure S12: Data analysis of the conductance of M2,  $V_{\text{bias}} = 170 \text{ mV}$ .

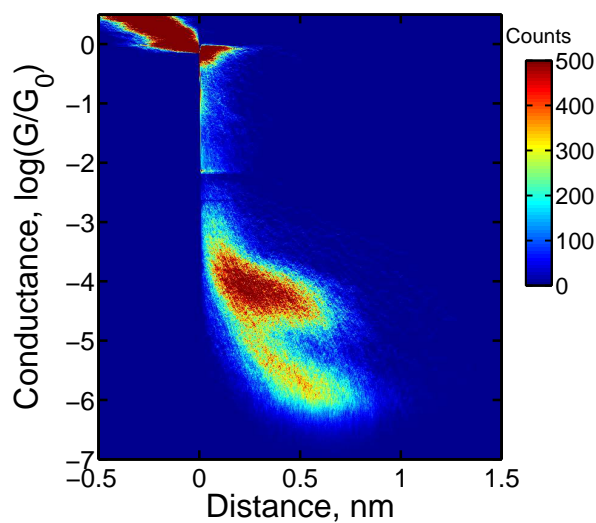
# Biphenyl dinitrile M3



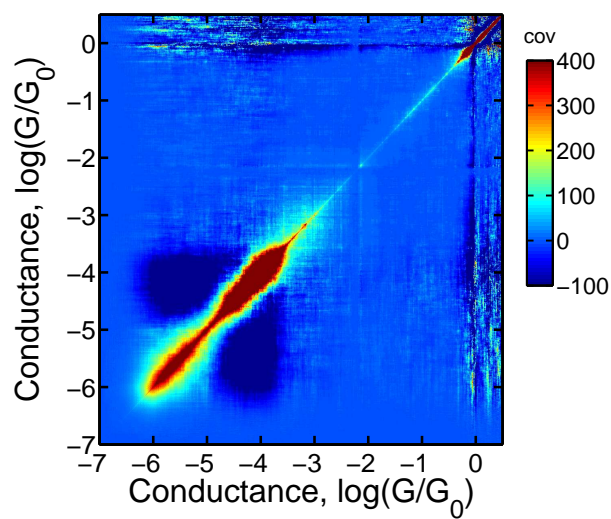
(a) Conductance histogram



(b) Characteristic length histogram

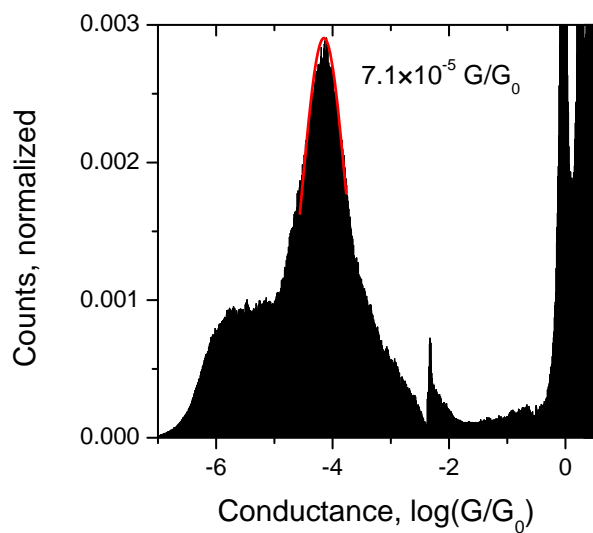


(c) 2D histogram

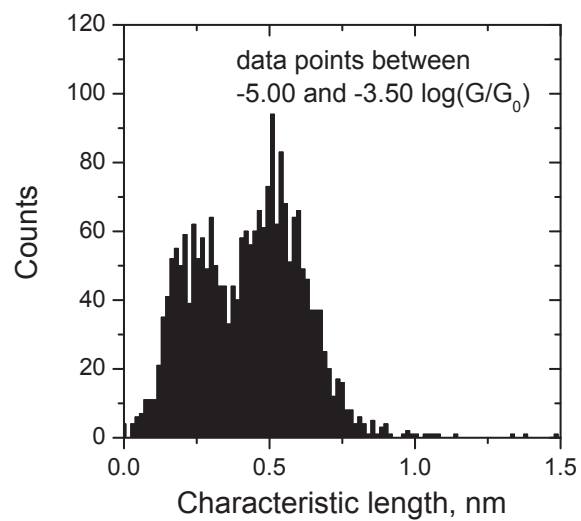


(d) Covariance matrix

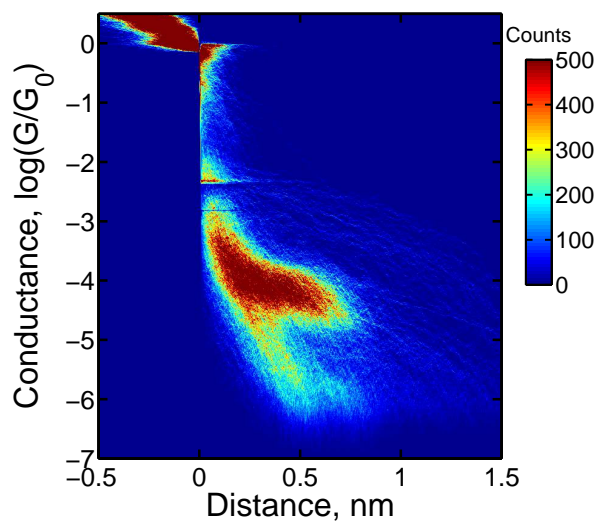
Figure S13: Data analysis of the conductance of M3,  $V_{\text{bias}} = 65$  mV.



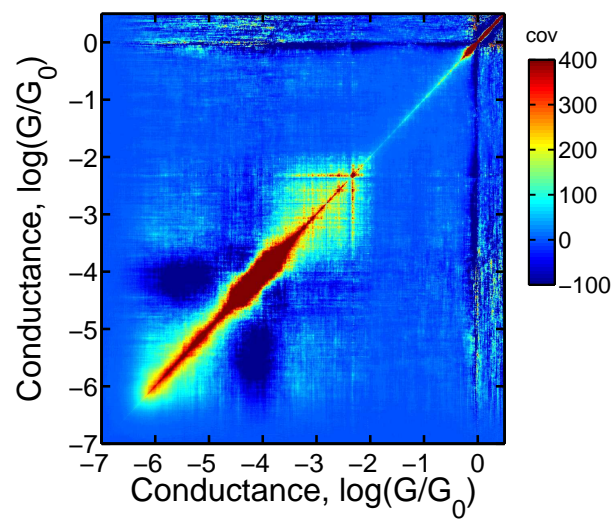
(a) Conductance histogram



(b) Characteristic length histogram

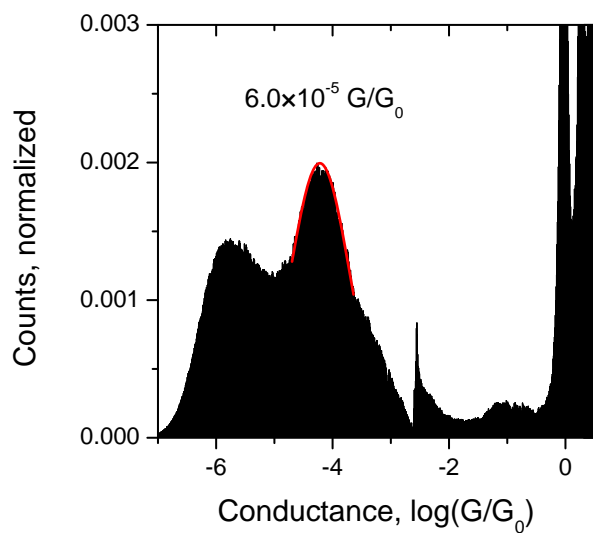


(c) 2D histogram

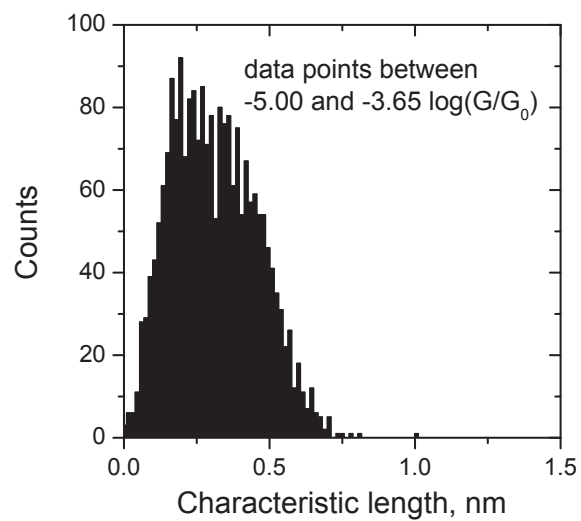


(d) Covariance matrix

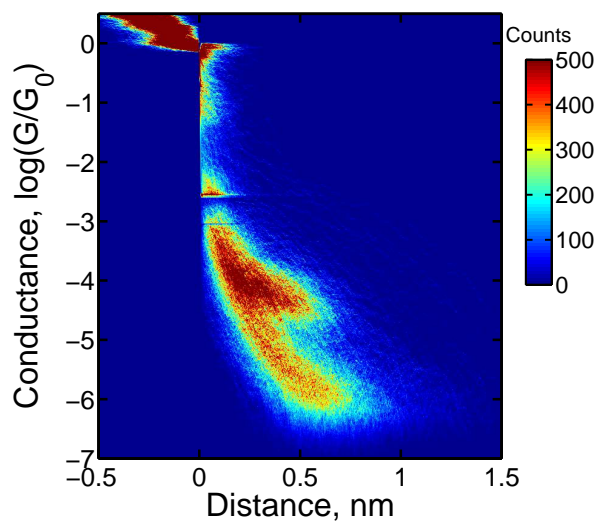
Figure S14: Data analysis of the conductance of M3,  $V_{\text{bias}} = 100 \text{ mV}$ .



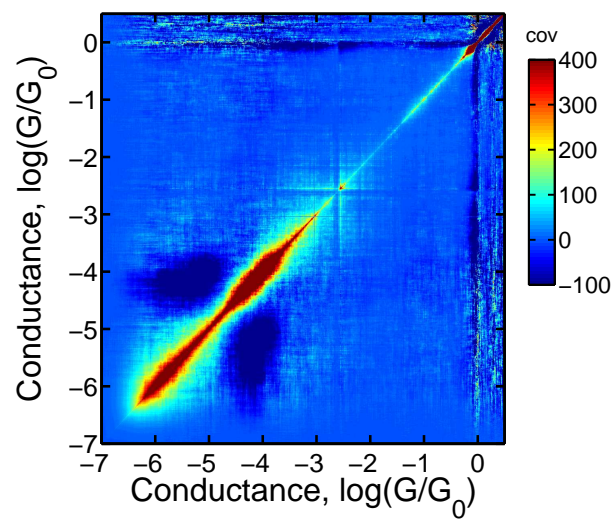
(a) Conductance histogram



(b) Characteristic length histogram



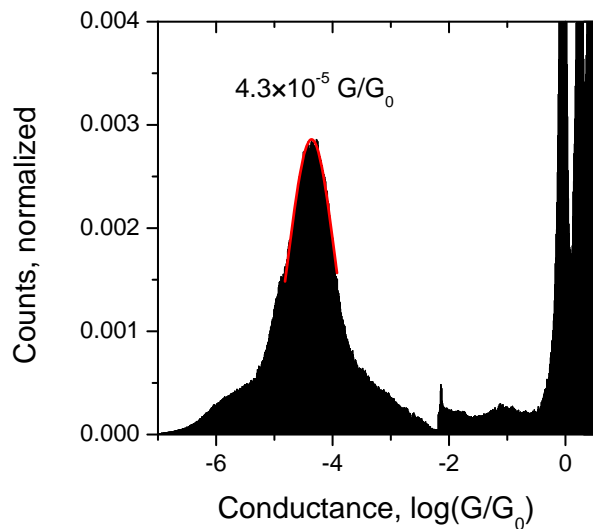
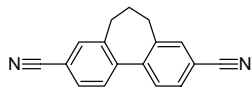
(c) 2D histogram



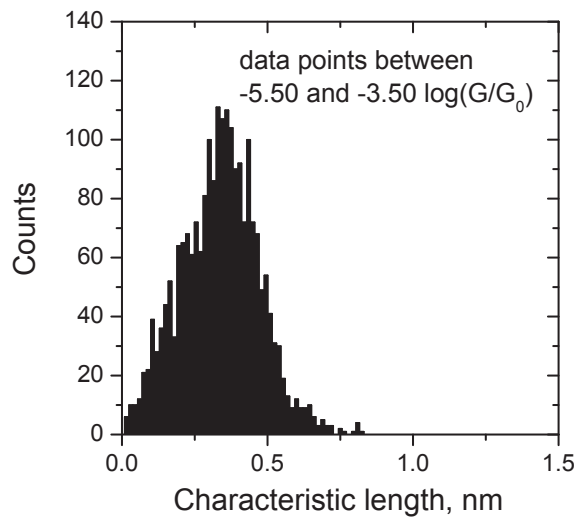
(d) Covariance matrix

Figure S15: Data analysis of the conductance of M3,  $V_{\text{bias}} = 170 \text{ mV}$ .

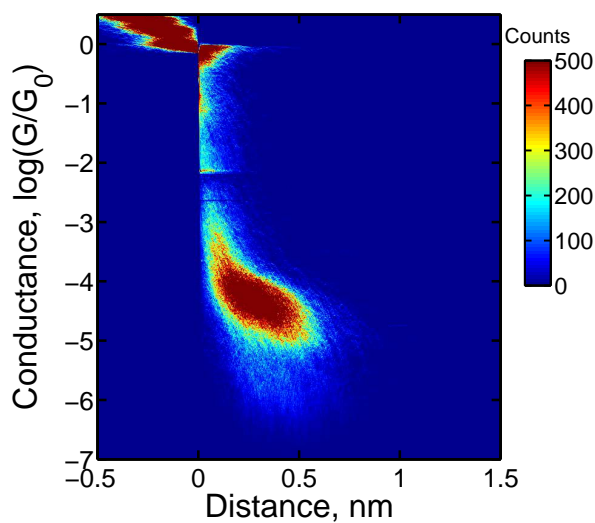
# Biphenyl dinitrile M4



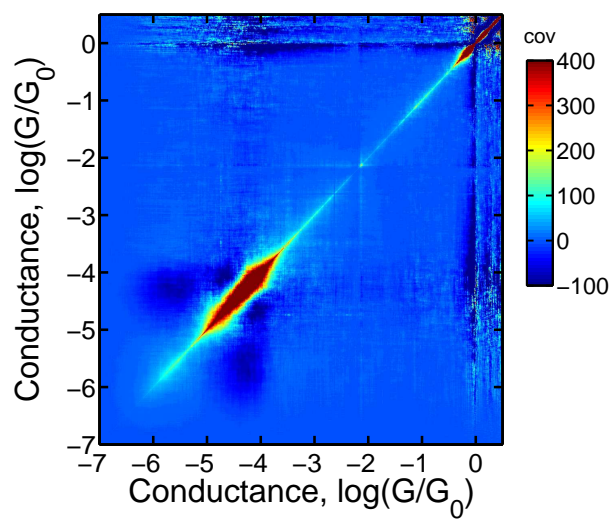
(a) Conductance histogram



(b) Characteristic length histogram

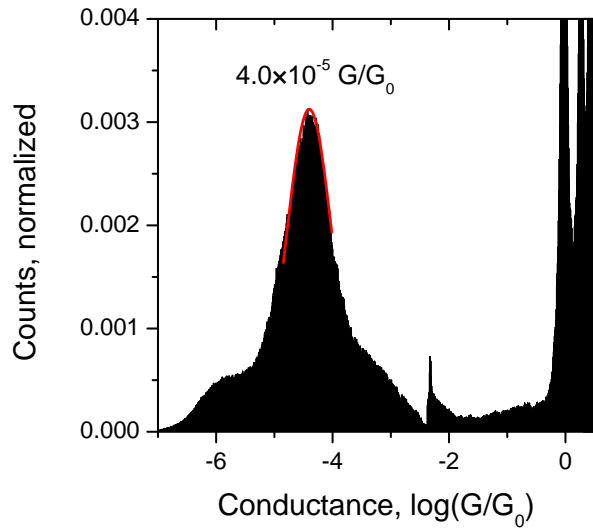


(c) 2D histogram

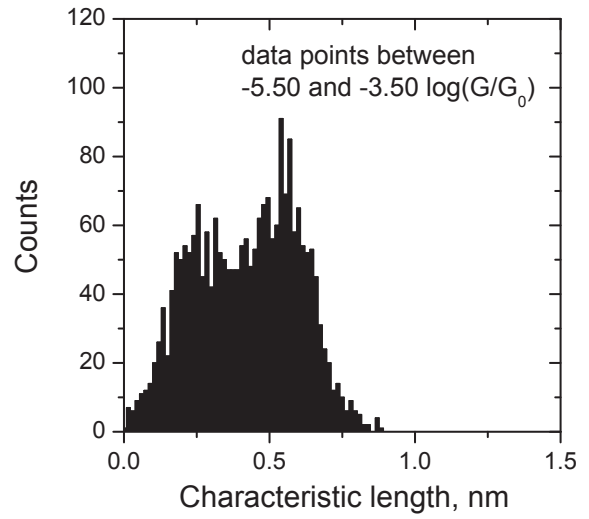


(d) Covariance matrix

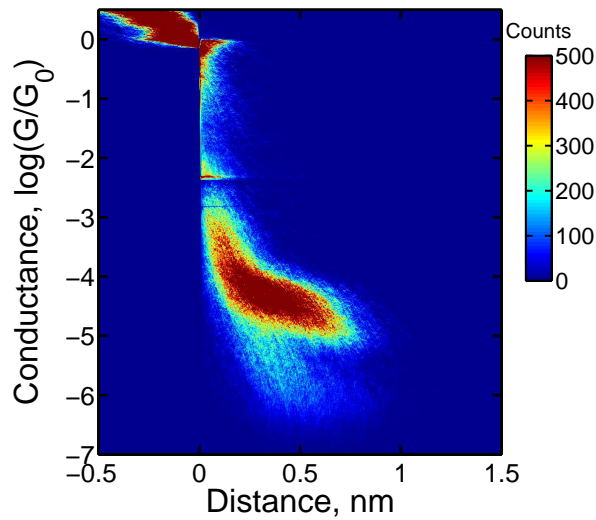
Figure S16: Data analysis of the conductance of M4,  $V_{\text{bias}} = 65$  mV.



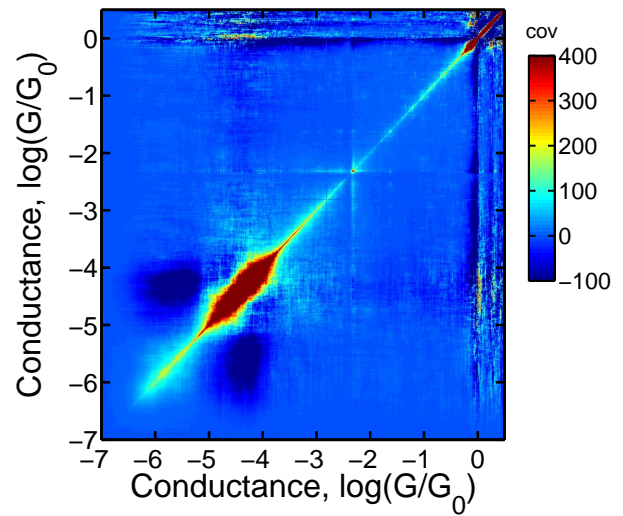
(a) Conductance histogram



(b) Characteristic length histogram

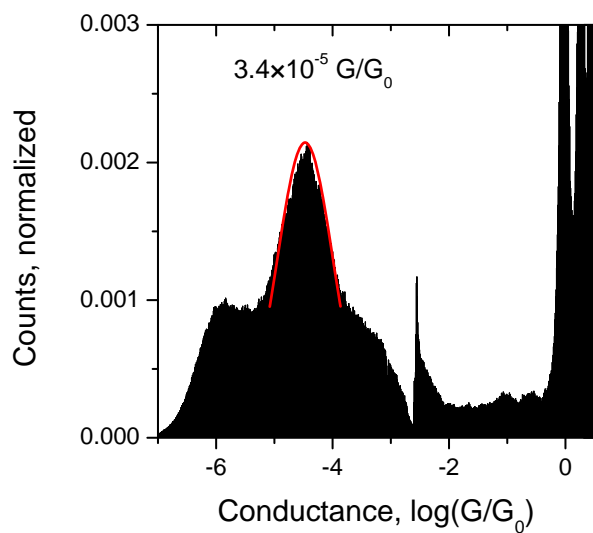


(c) 2D histogram

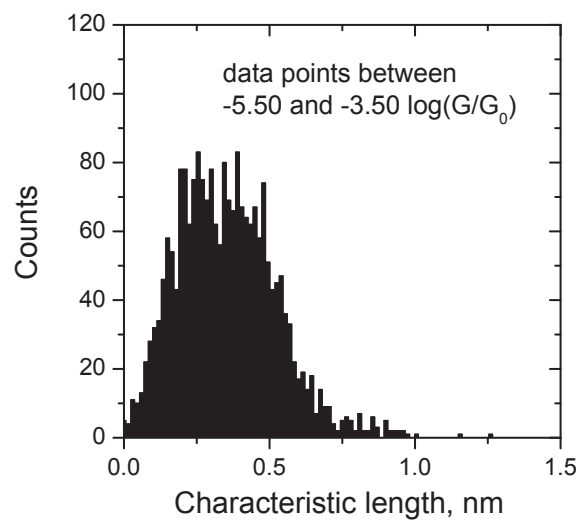


(d) Covariance matrix

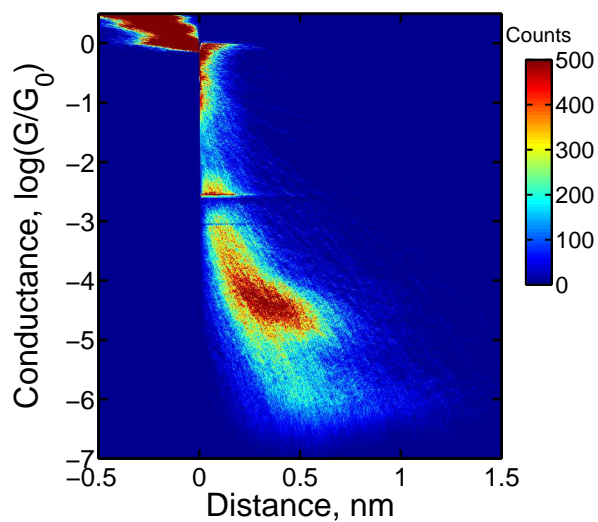
Figure S17: Data analysis of the conductance of M4,  $V_{\text{bias}} = 100 \text{ mV}$ .



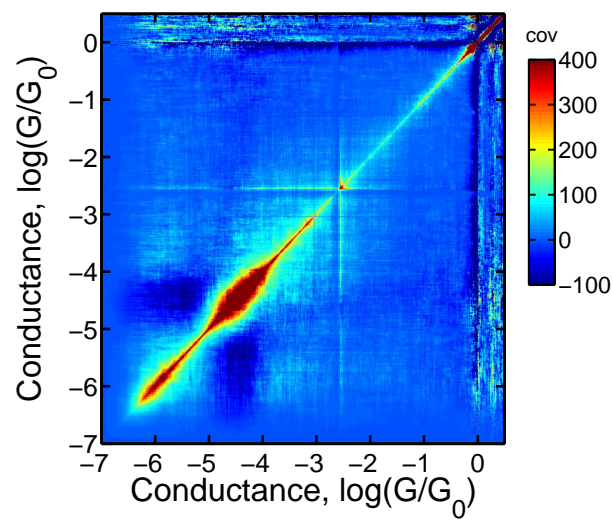
(a) Conductance histogram



(b) Characteristic length histogram



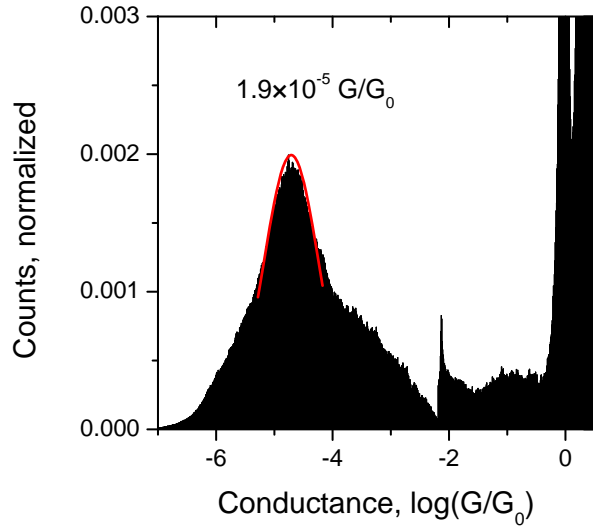
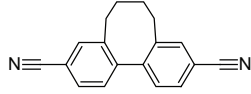
(c) 2D histogram



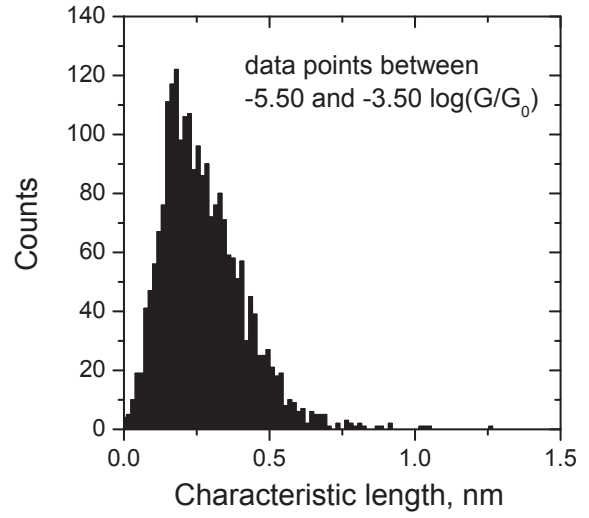
(d) Covariance matrix

Figure S18: Data analysis of the conductance of M4,  $V_{\text{bias}} = 170 \text{ mV}$ .

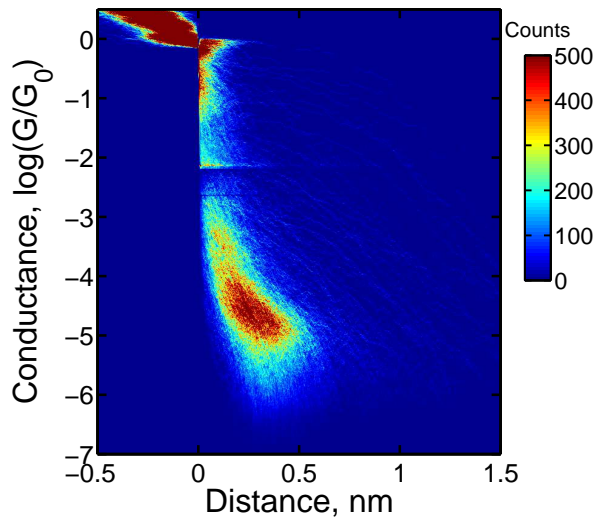
# Biphenyl dinitrile M5



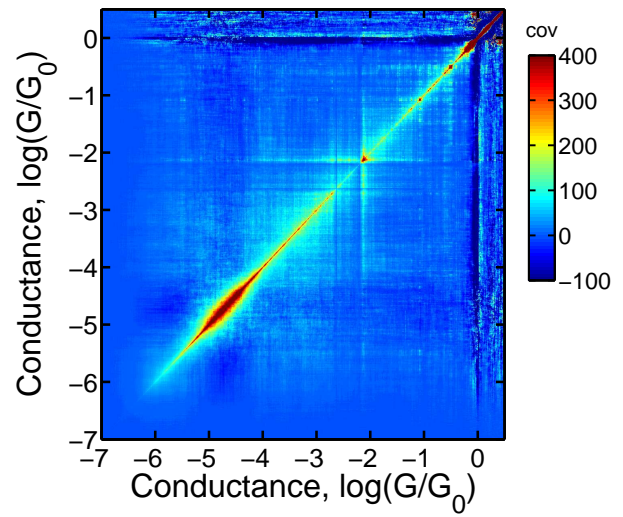
(a) Conductance histogram



(b) Characteristic length histogram

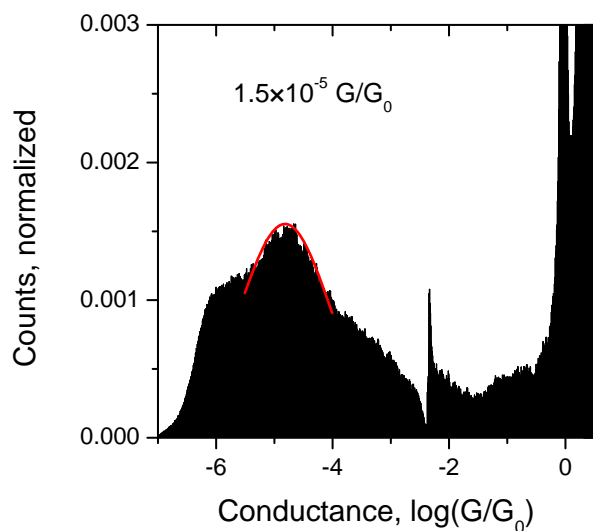


(c) 2D histogram

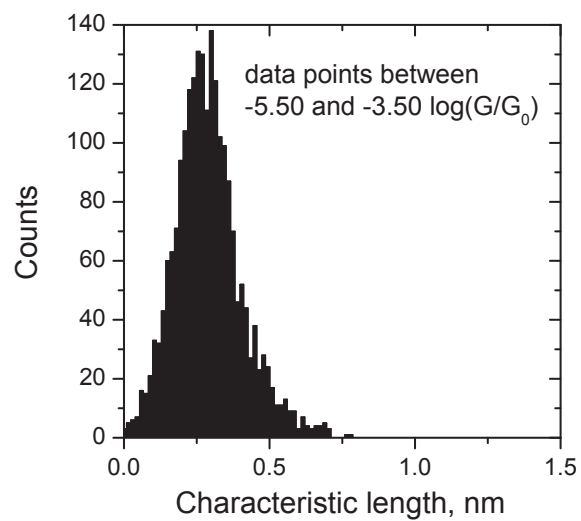


(d) Covariance matrix

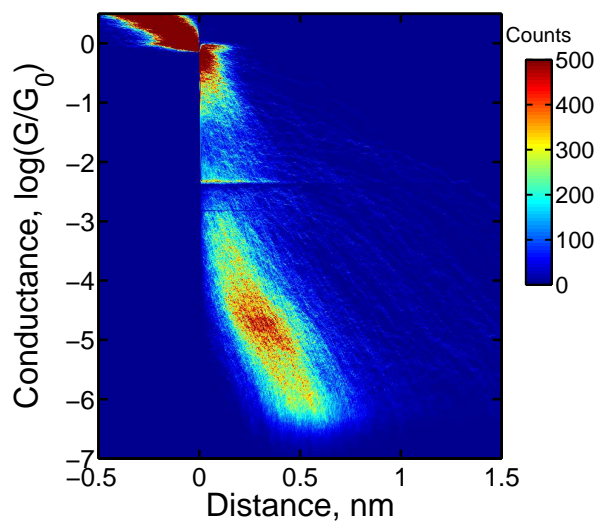
Figure S19: Data analysis of the conductance of M5,  $V_{\text{bias}} = 65$  mV.



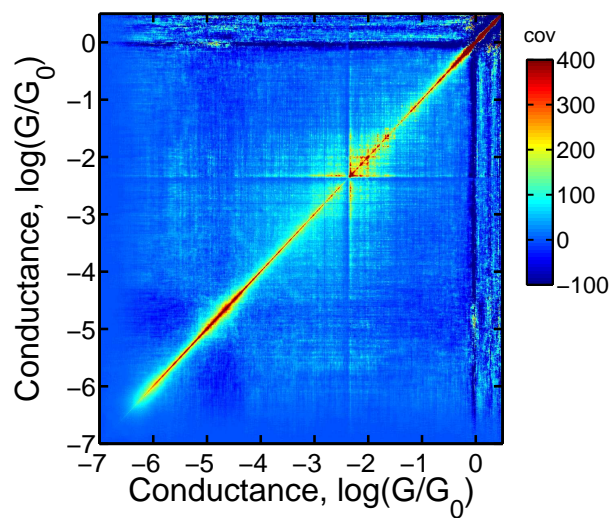
(a) Conductance histogram



(b) Characteristic length histogram

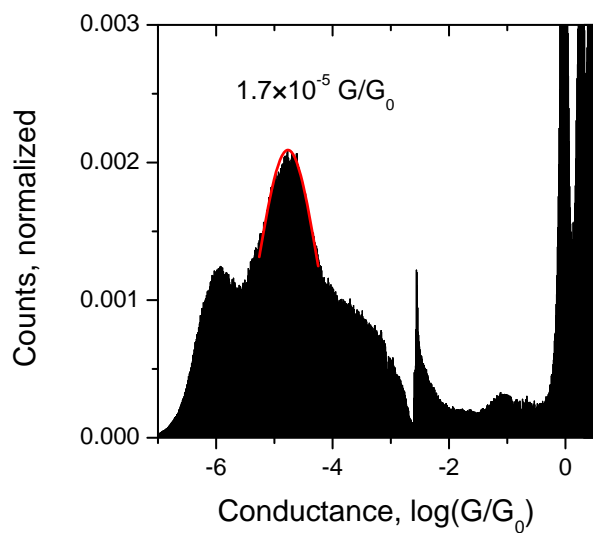


(c) 2D histogram

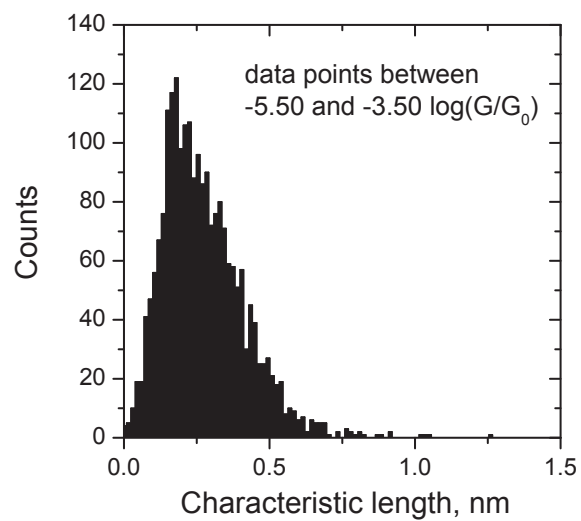


(d) Covariance matrix

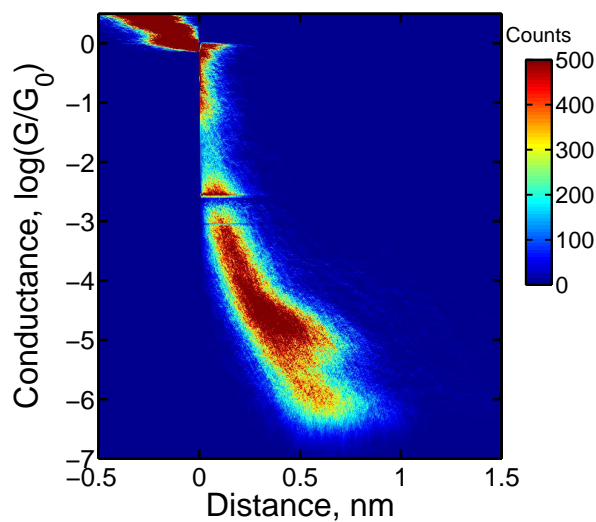
Figure S20: Data analysis of the conductance of M5,  $V_{\text{bias}} = 100 \text{ mV}$ .



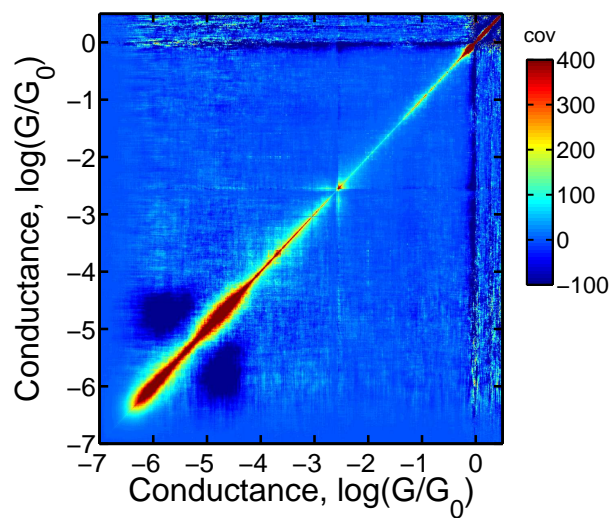
(a) Conductance histogram



(b) Characteristic length histogram



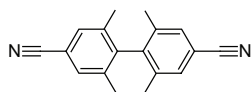
(c) 2D histogram



(d) Covariance matrix

Figure S21: Data analysis of the conductance of M5,  $V_{\text{bias}} = 170 \text{ mV}$ .

# Biphenyl dinitrile M6



# as compared with solvent

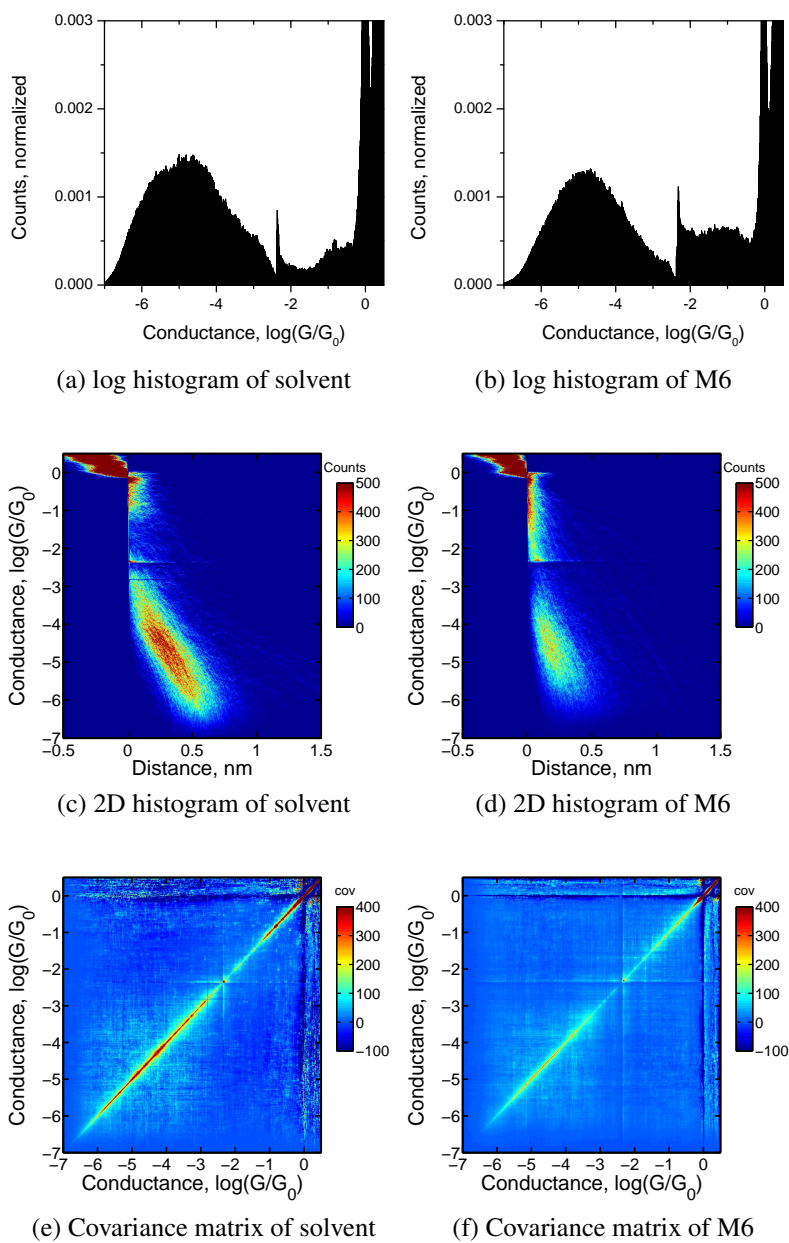


Figure S22: Data analysis of the conductance of M6 and of the solvent,  $V_{\text{bias}} = 100 \text{ mV}$ .

# Theoretical procedures

## Electronic structure and transport calculations

All electronic structure calculations in this work were performed within the framework of density functional theory (DFT) using the quantum chemistry software package TURBOMOLE.<sup>4</sup> Specifically, if not stated otherwise, we used a split valence basis set with polarization functions for all non-hydrogen atoms<sup>5</sup> and the BP86 exchange-correlation functional.<sup>6,7</sup> First, we analyzed all molecules in the gas phase. We optimized their geometric structures and obtained the corresponding ground state electronic structures. In Figure S23 we show the obtained positions of the frontier orbitals (HOMO and LUMO), where one can see a rather monotonic decrease of the HOMO-LUMO gap with decreasing torsion angle. This trend is confirmed by further calculations using the B3LYP exchange-correlation functional<sup>7,8</sup> and the Hartree Fock approach.<sup>9</sup> No particular feature was found which could justify the deviation observed experimentally for the fluorene molecule M2.

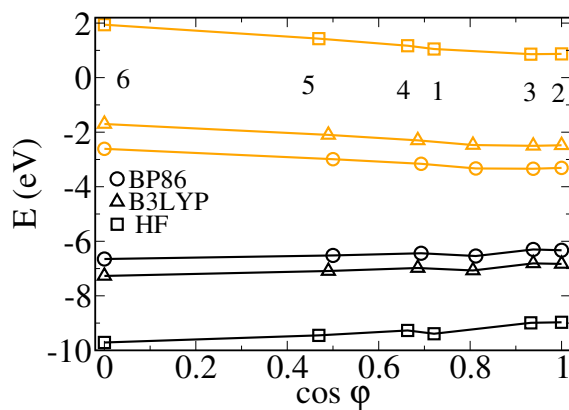


Figure S23: HOMO (black) and LUMO (orange) energies of all molecules as computed by three different methods (DFT with the BP86 and B3LYP functionals, and Hartree Fock).

To construct the molecular junctions, each molecule was firstly relaxed on top of a single 20-atom gold cluster grown along the  $\langle 111 \rangle$  direction. Then, a second cluster was attached to the other end and the whole structure was optimized again. In all optimizations, the two outermost layers in each cluster were kept fixed. As mentioned in the main text, two types of stable binding geometries (l.c. and h.c.) were studied. In Table S1, the corresponding binding geometries are

reported. They were found to be similar, with an average value of  $-1.05 \pm 0.02$  eV.

Table S1: Computed binding energies for the l.c. and h.c. geometries.

Molecule	Binding energies (eV)	
	l.c.	h.c.
M1	-1.03	-1.01
M2	-1.05	-1.03
M3	-1.06	-1.05
M4	-1.07	-1.04
M5	-1.07	-1.03
M6	-1.1	-1.04

The molecular torsion angles calculated in both types of junctions as well as for the “free” molecule in the gas phase are compared with the angles measured experimentally in Table S2. Notice the good agreement.

Table S2: Torsion angles measured by X-ray crystal structure analysis<sup>10</sup> and those obtained theoretically for molecules in the gas phase and inside the two types of stable molecular junction configurations.

Molecule	X-ray <sup>10</sup> $\varphi$ (deg)	DFT			
		gas phase, CN $\varphi$ (deg)	gas phase, H $\varphi$ (deg)	l.c. $\varphi$ (deg)	h.c. $\varphi$ (deg)
M1	not available	35.5	36.6	35.3	33.1
M2	1.0	0.2	0.1	0.1	0.7
M3	20.7	20.3	20.5	20.2	19.5
M4	44.8	46.3	46.5	46.4	45.1
M5	58.5	59.8	60.0	59.9	59.2
M6	89.3	90.0	90.0	90.0	89.6

After geometry optimization, the gold cluster size was extended to 120 atoms on each side for a proper description of the alignment of the molecular energy levels with respect to the Fermi energy. Single point calculations were performed on the resulting extended junctions. Then, the electronic transport characteristics were calculated by using the Green’s function technique and the Landauer formalism as described in our previous publication.<sup>11</sup> The transmission curves obtained for the l.c. geometries are shown in Figure S24 (see main text for those corresponding to the h.c. geometry). As in the h.c. geometries, the transport is largely dominated by the LUMO of the molecules.

For both binding geometries, our calculations reproduce the general trend of the conductance decrease with increase of the torsion angle. However we find slight deviations of the theoretical conductance values from the linear  $\cos^2 \varphi$  dependence. A possible reason might be the known inaccuracy of DFT in determining the energy of the molecular orbitals. The transmission curves are rather steep near the Fermi energy, and a small shift in  $(E_{\text{LUMO}} - E_{\text{F}})$  may translate into a big error in the conductance value, thus affecting the general trend.<sup>12,13</sup>

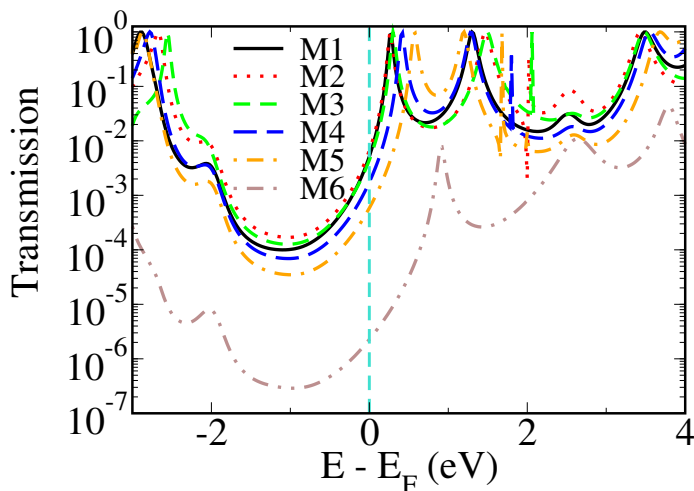


Figure S24: Computed transmission curves for M1 to M6 in the l.c. geometry.

In order to gain some further insight into the conduction through these molecular junctions, we have also analyzed the individual conduction channels. Let us remind that in the spirit of the Landauer approach the low temperature conductance can be written as a sum of independent contributions as follows

$$G = \sum_i G_i = G_0 \sum_i T_i(E_F), \quad (3)$$

where  $T_i(E_F)$  are the transmission coefficients at the Fermi energy defined as the eigenvalues of the transmission matrix. Within our Green's function formalism we have computed the contribution of the individual conduction channels for all the molecular junctions investigated in this work. In Figure S25(a-c) we show the transmission coefficients,  $T_i$ , as a function of energy for molecules M2, M3 and M6 in the l.c. geometry. In Figure S25(d) we report the contribution of the individual channels to the total conductance,  $G_i$ , for all the molecules in the l.c. geometry as a function of

$\cos^2 \varphi$ . Notice that for all the molecules, except for M6, the conductance is dominated by a single channel. In the case of M6, we find that two conduction channels give the same contribution around the Fermi energy. This is consistent with what was obtained in Ref. 13. Similar results are also obtained for the h.c. geometry.

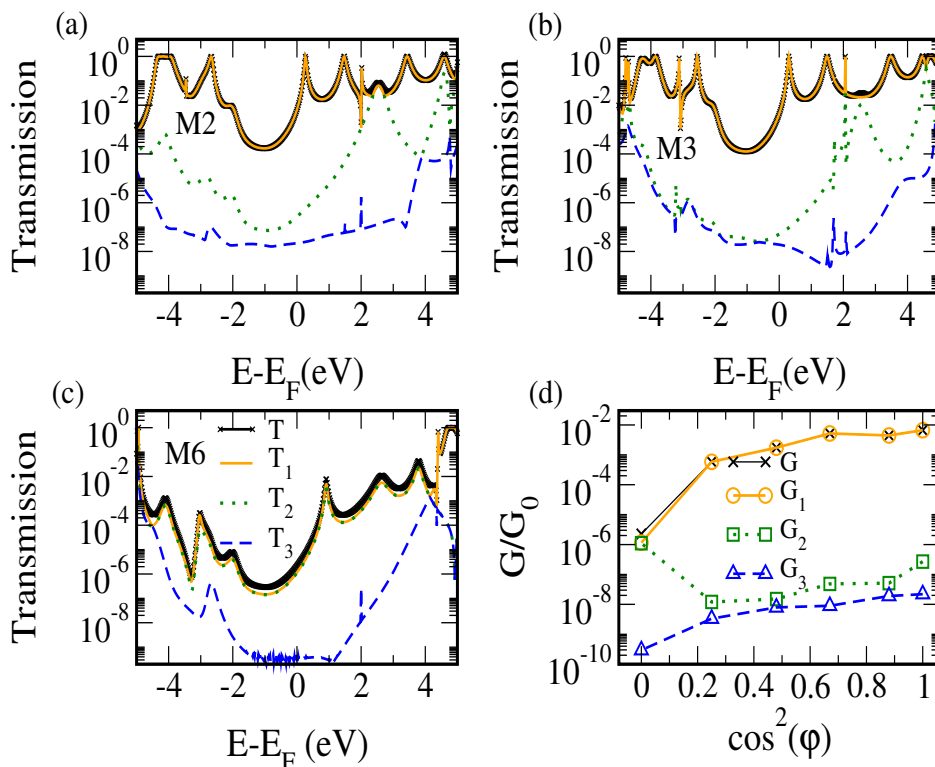


Figure S25: (a-c) Total transmission  $T$  and transmission coefficient  $T_i$  as a function of energy for molecules M2, M3 and M6 in the l.c. geometry. (d) Total conductance ( $G$ ) and individual channel contributions ( $G_i$ ) for all molecules in the l.c. geometry.

To establish the nature of the dominant conduction channels we have followed the procedure described in Ref. <sup>14</sup> to compute the wave functions associated with the different channels. In Figure S26 we display the wave functions of the dominant channels for molecules M2, M3 and M6 in the l.c. geometry. Notice for M3 (see Figure S26b) the wave function has a clear  $\pi$  character and its symmetry resembles that of the LUMO of the isolated molecule. Notice also that this wave function has no weight on the atoms of the side chain, which means that the states of this group do not participate in the electrical conduction through the molecule. For molecule M2 (see Figure S26a) the conduction channel has also a  $\pi$  character, but in this case the wave function has

also a certain weight on the side-group. This suggests that this group provides an additional path for the current. Therefore, since not all the current is flowing through the  $\pi$  bond between the phenyl rings, this molecule might not necessarily follow the cosine square law, as in the case of the other ones. However, it is not clear whether this peculiarity is enough to explain the anomalous experimental behavior of M2, especially, since we observe no particular feature in our conductance calculations. Finally, in the case of M6 (see Figure S26c-d), where the torsion angle is close to  $90^\circ$ , the channels have a mixed  $\pi$ - $\sigma$  character.

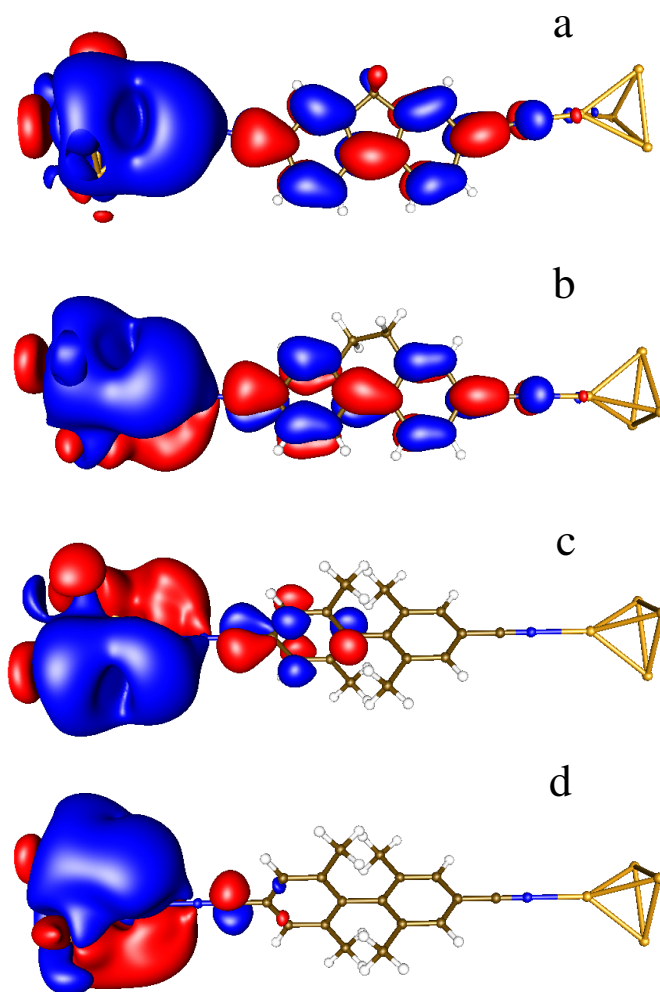


Figure S26: Wave functions of the dominant conduction channels at the Fermi energy for molecules M2 (a), M3 (b) and M6 (c-d) in the l.c. geometry.

## Molecular dynamics calculations

In order to explore the influence of temperature on the molecular conformation, we performed molecular dynamics (MD) simulations for the pristine (hydrogen terminated) molecules in both vacuum and solvent. The aim was to provide a more general understanding of the role of fluctuations in the torsion angle which can possibly be extended to the corresponding molecules with different types of anchoring groups. Our choice is justified by the observation of a weak dependence of the torsion angle on the terminal groups (see Table S2 and discussions in Ref.<sup>1</sup>).

MD simulations were performed by using the Leapfrog Verlet algorithm<sup>15</sup> as implemented in TURBOMOLE.<sup>4</sup> We proceeded along the lines of Frelek *et al.*<sup>16</sup> to set up our calculations. The temperature was set to 300 K by using the Nosé-Hoover thermostat;<sup>17</sup> 8000 time steps of 20 a.u. (0.48 fs) step length were carried out. The value of this time scale was obtained from a previous calculation of the vibrational energies of M1. More precisely, it was chosen to be no longer than 1/10 of its shortest vibrational period (11 fs or 3116.12 cm<sup>-1</sup>). The thermostat relaxation time was then set four times larger than the time step, while the total number of steps was chosen based on the time scale of the torsional molecular motion, which is of the order of a picosecond. To simulate the molecular motion in the presence of a solvent, the COSMO model<sup>18</sup> as implemented in TURBOMOLE was used and the value of the dielectric constant was set to the room temperature bulk value of mesitylene (2.26).<sup>19</sup>

In order to carry out a statistical analysis, we performed seven MD runs for each molecule, starting from different initial geometry configurations. They were extracted from a previously computed 8000-time-steps trajectory at 900 K, by selecting the geometries at every 1000th step, starting from 2000. For the final run at 300 K, the torsion angle was measured at each time step by the following procedure: the center of mass of each phenyl ring  $\vec{s}_X$  ( $X = 1, 2$ ) was calculated, based on the carbon atoms. Then, the planes, which fitted the two rings best, were calculated by a least squares fitting procedure. The vectors normal to the ring planes,  $\vec{n}_X$ , were projected onto the plane normal to  $\vec{d} = \vec{s}_2 - \vec{s}_1$ , where  $\vec{d}$  is the line which connects the two centers of mass. Finally, the torsion angle was calculated as that comprised between the projected vectors  $\vec{n}_{Xp}$ , specifically

$$\varphi = |\arccos(\vec{n}_{1p} \cdot \vec{n}_{2p})| \text{ with } \vec{n}_{Xp} = \vec{v}_{Xp}/v_{Xp}, \vec{v}_{Xp} = \vec{n}_X - (\vec{n}_d \cdot \vec{n}_X)\vec{n}_d, \text{ and } \vec{n}_d = \vec{d}/d.$$

We considered it necessary to adopt this procedure rather than measuring just the simple dihedral angle as formed by four selected carbon atoms, because the two phenyl rings quite often showed a certain deviation from the planar structure throughout the trajectories.

Histograms representing the normalized angle distributions were generated by taking only the last 6000 time steps of the runs at 300 K into account. The histograms obtained in the gas phase for each molecule are displayed in Figure S27, together with their corresponding standard deviations.

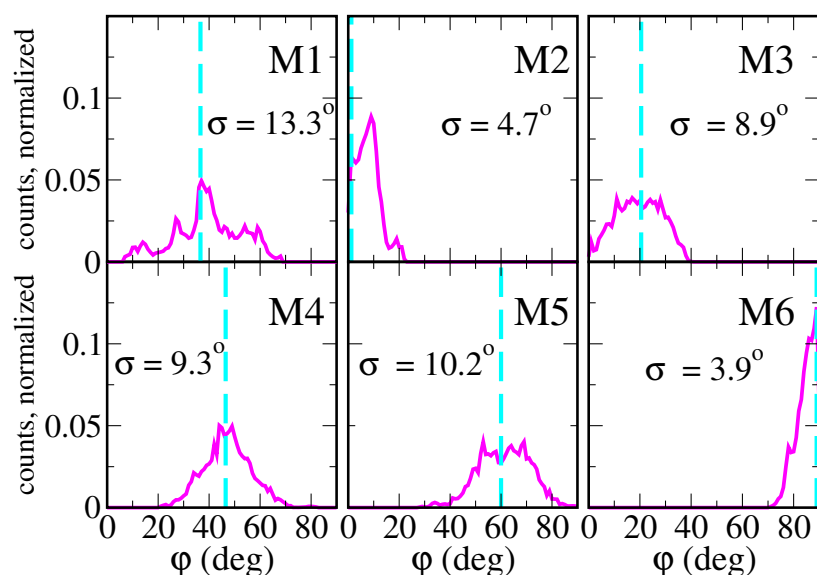


Figure S27: Torsion angle histograms obtained by MD calculations for all molecules. In every panel we indicate the corresponding standard deviation ( $\sigma$ ). The vertical dashed lines indicate the values of the static equilibrium angles.

Molecule M1 shows the largest fluctuation because there are no side chains which hinder the movement of the phenyl rings. On the contrary, molecules M2 and M6 are constrained, the former by a methylene group linking the two rings together, the latter by four methyl side groups which cause substantial steric hindrance. The other molecules exhibit somewhat more flexibility, due to longer side chains which can adjust to some extent upon ring rotation.

In order to estimate the impact of the angle variations on the conductance of the molecular

junctions, we determined the standard deviations for the conductance values from the relation

$$G(\varphi_i) = a \cos^2 \varphi_i, \quad (4)$$

where we consider torsion angles  $\varphi_i$  to vary within the standard deviations of the histograms in Figure S27. The same prefactor  $a$  for all molecules was chosen, using the values ( $5.9 \cdot 10^{-3} G_0$  and  $1.4 \cdot 10^{-2} G_0$  of the l.c. and h.c. geometry, respectively) as extracted from the fit of (Eq. (4)) to the DFT conductance values. The calculated deviations are reported as error bars in the conductance versus cosine square plot in Figure S28, where the conductance values are those obtained by DFT. In this graph, we have chosen to display the deviations of the conductance as a function of the cosine square of the fixed (zero-temperature) torsion angle in the gas phase obtained by DFT. We do not show the corresponding error bar for the angle itself. The reason for that is to establish a direct comparison with the experimental results, where the angle fluctuations due to either temperature or binding geometry are not known. As pointed out in the main text, the maximum deviation is found to be around 24% for M1. This value is however smaller than the variation due to a different binding geometry (140% for M1).

For completeness, MD simulations in the presence of solvent were also carried out. The histograms generated are rather similar to those obtained under vacuum conditions for all molecules. The largest, but still modest, deviations are observed for M1, where the distribution of the torsion angles is rather broad and the corresponding conductance deviation increases up to 26% (see Figure S29).

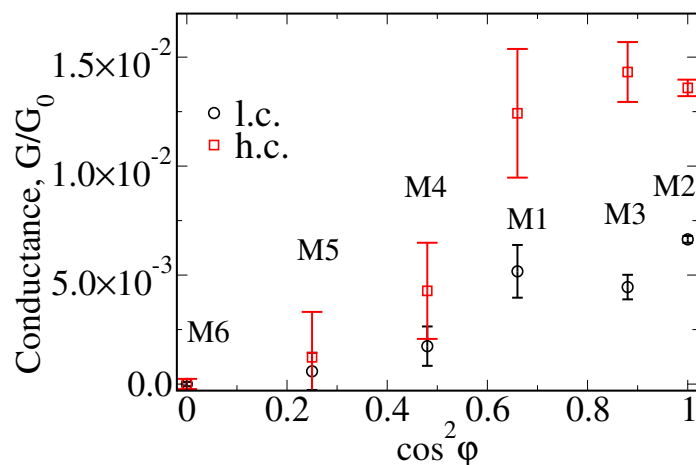


Figure S28: Conductance versus cosine square of the molecular torsion angle and the corresponding error bars as estimated from the MD simulations.

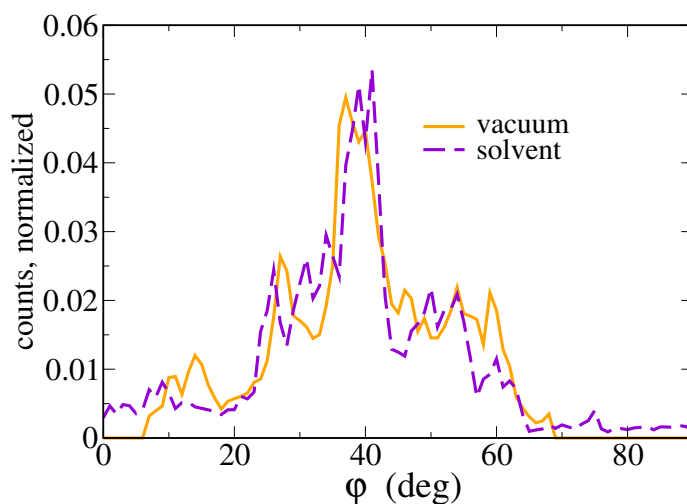


Figure S29: Torsion angle histogram for molecule M1 in vacuum and in mesitylene solution.

## References

- (1) Mishchenko, A.; Vonlanthen, D.; Meded, V.; Bürkle, M.; Li, C.; Pobelov, I. V.; Bagrets, A.; Viljas, J. K.; Pauly, F.; Evers, F.; Mayor, M.; Wandlowski, T. *Nano Lett.* **2010**, *10*, 156–163.
- (2) Meszaros, G.; Li, C.; Pobelov, I.; Wandlowski, T. *Nanotechnology* **2007**, *18*, 424004.
- (3) Halbritter, A.; Makk, P.; Mackowiak, S.; Csonka, S.; Wawrzyniak, M.; Martinek, J. *arXiv:1006.1811* **2010**, 1–5.
- (4) Ahlrichs, R.; Bär, M.; Häser, M.; Horn, H.; Kölmel, C. *Chem. Phys. Lett* **1989**, *162*, 165–169.

- (5) Schäfer, A.; Horn, H.; Ahlrichs, R. *J. Chem. Phys.* **1992**, *97*, 2571.
- (6) Perdew, J. P. *Phys. Rev. B* **1986**, *33*, 8822.
- (7) Becke, A. D. *Phys. Rev. A* **1988**, *38*, 3098.
- (8) Lee, C.; Yang, W.; Parr, R. G. *Phys. Rev. B* **1988**, *37*, 785.
- (9) Fock, V. *Z. Phys.* **1930**, *61*, 126.
- (10) Vonlanthen, D.; Rudnev, A.; Mishchenko, A.; Wandlowski, T.; Mayor, M. *Phys. Chem. Chem. Phys.* **2010**, *submitted*.
- (11) Pauly, F.; Viljas, J. K.; Huniar, U.; Häfner, M.; Wohlthat, S.; Bürkle, M.; Cuevas, J. C.; Schön, G. *New J. Phys.* **2008**, *10*, 125019.
- (12) Finch, C. M.; Sirichantaropass, S.; Bailey, S. W.; Grace, I. M.; and Colin J Lambert, V. M. G.-S. *J. Phys.: Condens. Mat.* **2008**, *20*, 022203.
- (13) Pauly, F.; Viljas, J. K.; Cuevas, J. C. *Phys. Rev. B* **2008**, *78*, 035315.
- (14) Paulsson, M.; Brandlbyge, M. *Phys. Rev. B* **2007**, *76*, 115117.
- (15) Verlet, L. *Phys. Rev.* **1967**, *159*, 98.
- (16) Frelek, J.; Kowalska, P.; Masnyk, M.; Kazimierski, A.; Korda, A.; Woznica, M.; Chmielewski, M.; Furche, F. *Chem. Eur. J* **2007**, *13*, 6732.
- (17) Hoover, W. G. *Phys. Rev. A* **1985**, *31*, 1695.
- (18) Klamt, A.; Schüürmann, G. *J. Chem. Soc. Perkin Trans.2* **1993**, *2*, 799.
- (19) Lide, D. R. *CRC Handbook of chemistry and physics, 90th edition*; 2009.